

Mechanical compaction mechanisms in the input sediments of the Sumatra Subduction Complex- insights from microstructural analysis of cores from IODP Expedition- 362

Sivaji Lahiri^{1*}, Kitty L. Milliken², Peter Vrolijk³, Guillaume Desbois¹, Janos L. Urai¹

¹Institute of Tectonics and Geodynamics, RWTH Aachen University, Germany, Lochnerstrasse 4–20, 52056, Aachen, Germany

²Bureau of Economic Geology, The University of Texas at Austin, Austin, TX, 10611, USA

³Department of Earth and Environmental Science, New Mexico Institute of Mining and Technology, 801 Leroy Place, Socorro, NM 87801, USA

* Corresponding author: sivaji.lahiri2@gmail.com

Abstract

The input sediments of the North Sumatra subduction zone margin, drilled during IODP Expedition 362, exhibit remarkable uniformity in composition and grain size over the entire thickness of the rapidly deposited Nicobar Fan succession (seafloor to 1500 mbsf), providing a unique opportunity to study the micromechanisms of compaction. Samples were prepared from dried core samples from sites (U1480 and U1481) by both Ar-ion cross-section polishing and broad-ion beam cutting and imaged with a field-emission Scanning Electron Microscope (SEM). The shallowest samples (seafloor to 28mbsf) display a sharp reduction in porosity from 80% to 52% due to collapse of large clay-domain/matrix pores associated with rotation and realignment of clay-platelets parallel to the bedding plane. The deeper succession (28mbsf to 1500mbsf) exhibits less rapid reduction in porosity from 52% to 30% by the progressive collapse of silt-adjacent larger pores through bending and subsequent sliding/fracturing of clay particles. In addition, there is a correlated loss of porosity in the pores too small to be resolved by SEM.

Clastic particles show no evidence of deformation or fracturing with increasing compaction. In the phyllosilicates, there is no evidence for pressure solution or recrystallization: thus, compaction proceeds by micromechanical processes. Increase in effective stress up to 18 MPa (~1500mbsf) causes the development of a weakly aligned phyllosilicate fabric mainly defined by illite clay particles and mica grains, while the roundness of interparticle pores decreases as the pores become more elongated. We propose that bending of the phyllosilicates by intra-particle slip may be the rate-controlling mechanism.

30 Pore size distributions show that all pores within the compactional force chain deform, irrespective of size, with
31 increasing compactional strain. This arises because the force chain driving pore collapse is localized primarily
32 within the volumetrically dominant and weaker clay-rich domains; pores associated with packing around isolated
33 silt particles enter into the force chain asynchronously and do not contribute preferentially to pore loss over the
34 depth range studied.

35 Introduction

36 Muds are fine-grained sediments (>50% of particles <63µm diameter) comprising platy detrital clay minerals and
37 equidimensional detrital grains such as quartz, feldspar, calcite, etc. (Nakano, 1967; Hesse, R., 1975; Sintubin,
38 1994). Understanding the mechanical, chemical, and microstructural properties of mud and mudstone is of great
39 interest for rock property prediction in basic earth science, in exploration, subsurface integrity studies and
40 geotechnical engineering (Yagiz, S., 2001; Aplin and Macquaker, 2011; Lazar et al., 2015). The chemical and
41 physical behavior of marine muds plays a critical role in defining the geometry of accretionary prisms, locating
42 the décollement for fault rupture (Vrolijk, 1990; Chester et al., 2013) and understanding subduction zone
43 earthquakes and tsunamis (Dean et al., 2010; Chester et al., 2013; Hüpers et al., 2017).

44 Marine mud is deposited with a highly porous isotropic fabric (Bowles, 1969; Bennett et al. 1981; 1991);
45 depositional porosity in mud is about twice as high as in sand (e.g., Velde, 1996, Lundegard, 1992). In contrast,
46 mudstones have low porosities, modal pore sizes measured in nm, and an absence of textural controls on porosity
47 (e.g. Aplin et al., 2006; Milliken et al., 2012; 2013). The processes in this dramatic evolution of porosity have
48 similarities to compaction of sand to sandstone, comprising a combination of compaction and cementation
49 (Milliken and Day-Stirrat, 2013), although the much smaller, elongated phyllosilicate grains increase the role of
50 clay-bound water in the process (Karaborni et al., 1996). Whereas a refined and somewhat predictive
51 understanding exists for porosity evolution in sand and sandstones (e.g., Lander and Walderhaug, 1999; Paxton et
52 al., 2002; Lander et al., 2008; Ajdukiewicz and Lander, 2010, Desbois et al., 2011), such a model is at best
53 preliminary for muds and mudstones (Pommer and Milliken, 2015; Milliken and Olson, 2017). It seems clear that
54 the composition of the grain assemblage importantly sets the stage for porosity evolution in muds (Milliken, 2014),
55 cementation being the greatest in muds with abundant biogenic debris. In contrast to sandstones, however,
56 cementation is far less common globally in mudstones (Milliken, 2019), leading to the notion that mechanical
57 compaction may be far more important in muds. In addition, depositional environment also strongly controls
58 porosity evolution, compaction and diagenesis in mudrocks (e.g. Burland, 1990; Baruch et al., 2015; Delle Piane
59 et al., 2015) as the initial clay and rigid grain compositions significantly affect both compaction (as this manuscript
60 shows) and subsequent diagenetic alteration due to variations in composition. Establishing the expected
61 compaction behavior for muds in a setting of well-constrained mud properties is an essential contribution that our
62 study hopes to serve.

63 Investigations of mud and mudstone compaction are usually based on proxy data, such as velocity or density,
64 rather than direct measurements of porosity (e.g., references in Mondol et al., 2007). Direct measurement of
65 porosity is broadly classified into two categories: 1) **experimental compaction in the laboratory**; (e.g., Mitchell,
66 1956; Bennett et al. 1981; Griffiths and Joshi, 1989; 1990; Vasseur et al. 1995; Mondol et al. 2007; Fawad et al.

67 2010; Emmanuel and Day-Stirrat, 2012), and 2) studies on natural samples those are compacted in situ with depth
68 (e.g., Meade, 1964; Ho et al., 1999; Aplin et al. 2003; 2006; Day-Stirrat et al., 2008; 2010; 2012; Milliken et al,
69 2012; 2013). A common shortcoming of the studies on the naturally compacted samples is the assumption that the
70 bulk porosity is a direct measure of compaction although porosity loss has contributions of both compaction and
71 cementation (Ehrenberg, 1989; Lundegard, 1992; Paxton et al., 2002), and this can only be accomplished by
72 petrographic inspection (Milliken and Curtis, 2016). Experimental studies generally avoid this shortcoming as the
73 sample sets generally do not undergo any chemical change during the investigation. Studies of shallowly buried
74 units (like the present study) are the ones most likely to avoid the complication of cementation, especially if
75 temperatures are low and bulk grain assemblages are siliciclastic (Milliken, 2008, 2014).

76 Previous studies report contrasting ideas about the mechanisms of mechanical compaction of mud. Some studies
77 conclude that rotation is the dominant particle scale mechanism for mechanical compaction (Bowles et al., 1969;
78 Oertel and Curtis, 1972; Vasseur et al., 1995), although other particle scale-deformation mechanisms were not
79 investigated by these authors. A few studies state that burial compaction significantly increases the alignment of
80 phyllosilicate (clay and mica) parallel to the bedding planes (Bowles et al., 1969; Oertel and Curtis, 1972; Vasseur
81 et al., 1995) (a detailed review of the previous studies on mechanical compaction is given in Document S1 in
82 Supplementary data). Other studies suggest that intense mechanical compaction (i.e. effective stress) has a limited
83 impact on the development of phyllosilicate fabric in mud (Ho et al., 1999; Aplin et al., 2006; Day-Stirrat et al.,
84 2008; 2011). In addition, earlier authors concluded that an increase in effective stress causes preferential loss of
85 larger pores, and as a result, the mean porosity of the samples decreases (Delage and Lefebvre, 1984; Griffiths and
86 Joshi, 1989; 1990; Emmanuel and Day-Stirrat, 2012). With increasing consolidation stress, a bimodal pore size
87 distribution curve shifts toward smaller pore sizes as larger pores rapidly collapse (Griffiths and Joshi, 1989; 1990;
88 1991). These studies investigated the changes in particle alignment and reduction in porosity (Ho et al., 1999;
89 Aplin et al., 2006; Day-Stirrat et al., 2008; 2011) but without imaging the evolution of pore morphology with
90 increasing compactional strain. Moreover, in previous studies, the authors mainly performed laboratory
91 consolidation experiments on lab produced particle packs, and used conventional techniques, such as mercury
92 intrusion porosimetry and high-resolution X-Ray pole figure goniometry (HRXTG) to understand the evolution of
93 pore size distribution with consolidation stress (Ho et al., 1999; Aplin et al., 2006). Studies on naturally compacted
94 samples are less common.

95 We received 55 mud samples from drill cores collected during IODP Expedition 362 west of the North Sumatra
96 subduction zone margin and investigated the evolution of petrographic microstructure and pore morphology as a
97 function of compactional strain. Apart from general implications for global mudrocks, we hope this investigation
98 will also contribute to studies that seek to predict rock properties in the deeper subsurface at the Sumatra
99 subduction front.

100

101 Geological background and drilling

102 The Sumatra subduction zone extends 5000km from the Andaman-Nicobar Islands in the northwest to the Java-
103 Banda arc in the Southeast (Fig.1a and b) (Prawirodirdjo et al., 1997; Hippchen and Hyndman, 2008). The trench
104 of the Sumatra subduction zone (Fig.1a) developed on the subducting Indo-Australian Plate at a convergence rate
105 of 5.5 cm/yr in the north and 7.23 cm/yr in the South (Ghosal et al., 2014; Moeremans, and Singh, 2015).

106 On 26th December 2004, the west coast of Northern Sumatra recorded one of the largest earthquakes (Mw-9.3) in
107 the 21st century, generating a devastating tsunami in the Indian Ocean (Ammon et al., 2005; Lay et al., 2005).
108 Understanding the mechanism(s) behind this unprecedented event was the central idea behind IODP Expedition
109 362 (Fig.1). The main objective of the expedition was to collect core and log data from the incoming sedimentary
110 succession of the Indo-Australian oceanic plate to understand the seismogenic process related to the margin (Dugan
111 et al., 2017; McNeill et al., 2017a). During the expedition in 2016, drilling was performed on two sites: U1480
112 (Holes E, F, G and H) and U1481 (Hole A) located on the oceanic plate west of the North Sumatra subduction
113 margin and east of the Ninety East Ridge (Fig.1a, b) (Dugan et al., 2017). The drilling sites recovered a complete,
114 1.5 km thick sedimentary section from late Cretaceous to Pleistocene down to the basement of basaltic crust
115 (Dugan et al., 2017; McNeill et al., 2017a).

116 The input sedimentary section of the Sumatra subduction zone comprises the distal part of the trench wedge,
117 Nicobar fan sequence, and pre-fan pelagic section on the basaltic crust at the bottom (Dugan et al., 2017; McNeill
118 et al., 2017a). At Site U1480, the entire recovered section was categorized into six lithological entities, Units I to
119 VI (Fig. 1c) (McNeill et al., 2017a). Unit I (0 to 26.72 mbsf) consist of unconsolidated calcareous clay, silty clay
120 with alternating fine sand (McNeill et al., 2017a). Unit II from 26.72 to 1250 mbsf consists of three subunits (IIA,
121 IIB and IIC) and mainly exhibits alternating fine-grained sand and silty clay to silt (McNeill et al., 2017a). Unit
122 III (1250 ~ 1327 mbsf) is divided into two subunits: Unit IIIA and IIIB (McNeill et al., 2017a). Unit IIIA consist
123 of thin to medium-bedded, gray-green or brown mudstone and intercalated siltstone, and Unit IIIB is composed of
124 reddish-brown tuffaceous silty claystone with fragmented sponge spicules and radiolaria (McNeill et al., 2017a).
125 The boundary between Units IIIA and IIIB (1310 mbsf) at this site marks the base of the Nicobar Fan and the
126 beginning of the thin pre-fan succession (Pickering et al., 2020). Units IV, V, and VI include volcanoclastic rocks
127 with tuffaceous sandstone, conglomerates, and basaltic oceanic crust, respectively. At Site U1481, the pre-fan
128 succession was not encountered and a Unit III, a thicker equivalent of Subunit IIIA at Site U1480, represents the
129 material of the lower Nicobar Fan (see Figure F15, in Site U1481 report; McNeil et al., 2017a). This study is
130 restricted to the thin, distal trench wedge (Unit I) and Nicobar fan sequence (Units II and IIIA, which is equivalent
131 to Unit-III at U1481).

132 X-ray diffraction (XRD) of bulk samples and clay fractions at Site U1480 show a clay mineral assemblage
133 dominated by illite with lesser amounts of smectite and chlorite (Rosenberger et al., 2020) (Fig.2a, b, c, and d;
134 Table S1 and Figure S1 in Supplementary data). Clay mineral data arise from three separate analyses: (1) bulk
135 sample analyses of air-dried samples (random orientation) onboard ship used to define the proportion of all clay
136 minerals in a sediment sample (McNeill et al., 2017a), (2) air-dried clay-sized samples (sedimented and oriented)
137 analyzed in New Mexico that define the types and abundances of clay minerals (Rosenberger et al., 2020; note

138 that abundances limited to clay minerals used in the reference mixtures, which include discrete illite and discrete
139 smectite), and (3) glycol-saturated clay-sized samples (sedimented and oriented) analyzed in New Mexico that
140 determine the amount of illite in mixed-layer I/S, defined as smectite in #2 (Rosenberger et al., 2020). Note that
141 the amount of illite in mixed-layer I/S is only accounted for in the expandability value and never in the discrete
142 illite value.

143 Siliciclastic samples consist of 50-70% clay minerals (McNeill et al., 2017a). Smectite fraction, determined from
144 the air-dried, clay-sized samples (as described in Underwood et al., 2020) is more abundant in Unit I than Unit II,
145 where smectite abundance ranges from 5-30% with rare samples containing as much as 45% smectite. In Unit II,
146 smectite fraction ranges from 10-30% with local discrete enrichments as great as 40-45%. Smectite again increases
147 in Unit III, reaching a value as high as 68% in the samples attributed to the Nicobar Fan section. There is a weak
148 increase in the expandability of mixed-layer I/S with depth (determined from glycol-saturated, clay-sized samples;
149 Rosenberger et al., 2020; Underwood et al., 2020; Figure-S2 in Supplementary data), suggesting a shift in clay
150 mineral provenance rather than smectite-illite diagenesis. Montmorillonite is interpreted as the smectite mineral
151 (Rosenberger et al., 2020). Chlorite + kaolinite abundance is similar in Units I and II, ranging from 8 to 20% with
152 rare occurrences as high as 24%; Unit III is almost devoid of chlorite + kaolinite. Heating experiments on select
153 samples indicate that chlorite makes up 66-100% of this mineral category (Rosenberger et al., 2020). Illite
154 comprises the remainder of the clay mineral assemblage, ranging from 50-79% in Unit II while Unit I is
155 correspondingly less illite-rich (42-70%). In the Unit III Nicobar Fan section, illite makes up only 18-36% of the
156 clay fraction. Again, it should be noted that, the shipboard methodology used for XRD analysis is semiquantitative
157 and has limitations in identifying bulk mineralogy of the samples; the abundance of mixed-layer clays and the
158 expandability of mixed-layer I/S is only inferred qualitatively (McNeil et al. 2017a; Underwood et al., 2020).

159 The Nicobar fan sequence exhibits almost compositionally homogeneous (silt/clay ratio; mostly 'silty-clay')
160 subunits with uniform grain size (McNeill et al., 2017a), and a history of rapid deposition (125-290 m/my;
161 Backman et al., 2019). The sedimentary sequence exhibits no evidence of uplift and currently occurs at maximum
162 burial depth. The drilling sites are 255 km away from the deformation front; thus, the samples are undisturbed by
163 tectonic faulting associated with subduction (Fig.1b). In addition, owing to the scarcity of biogenic grains and the
164 low temperatures encountered (<68°C), cementation is only observed as highly localized concretions (Red colored
165 symbols in Fig.2e, f, g, and h) (McNeil et al., 2017b; Torres et al., 2022). Such a homogeneous sedimentary
166 succession extending across 1.5 km depth is rare in sedimentary basins. Hence, these samples provide us with a
167 unique opportunity to study depth-wise variation in microstructure as a function of vertical effective stress with
168 few complications from multiple causes of porosity loss.

169 Sampling and Methods

170 This study is based on two sample sets that were obtained from Sites 1480 (Holes E, F, G, and H) and 1481 (Hole
171 A) independently and analyzed by slightly different methods. Samples have been prepared using Ar-ion cross-
172 section polishing and analyzed using a scanning electron microscope equipped with a field emission gun (BIB-SE
173 technique). The first sample set (33 mud samples; depth 1.24 to 1300 mbsf) was prepared and analyzed at RWTH
174 Aachen University, Germany. The second sample set (22 samples; depths 6.25 to 1493.30 mbsf) was prepared and

175 studied at the Bureau of Economic Geology (BEG) at the University of Texas at Austin. Respective core
176 description of these 55 mud samples and their bulk mineralogy data are tabulated in Table-1.

177 BIB-SEM technique (First set of samples, Aachen University)

178 Sample preparation for BIB-SEM and imaging

179 After drilling, the samples were stored at Kochi drill core repository (IODP), Japan for four years (2016 ~ 2020)
180 in refrigerated storage areas, maintaining a temperature of ca. 4°C and 80% humidity ([http://www.kochi-](http://www.kochi-core.jp/en/iodp-curation/curation-sop_2.html)
181 [core.jp/en/iodp-curation/curation-sop_2.html](http://www.kochi-core.jp/en/iodp-curation/curation-sop_2.html)). We received a total of 33 freeze-dried mud samples (SN-1 to SN-
182 33 in Table-1) for analysis at Aachen. The samples were collected using a tube inserted perpendicular to the cut
183 face of the drill core in such a way that the notch of the tube identified the top of the sample so the orientation of
184 bedding planes for each sample was known. In Fig. 1d, a tube sample received from the IODP repository is shown,
185 where the red line on the top of the tube identifies the notch. Subsamples ($10 \times 5 \times 2 \text{ mm}^3$) were cut from the
186 individual freeze-dried samples using a razor blade. These subsamples were pre-polished using silicon carbide
187 (SiC) paper to reduce the roughness of the surface down to 10 μm . Further, Broad Ion Beam (BIB) polishing was
188 carried out using a JEOL SM-09010 cross-section polisher for 10 hours at 6 kV and 150 μA . BIB reduces surface
189 damage by removing a 100 μm thick layer to generate a high-quality polished cross-section of 1-2 mm^2 with a
190 topography less than 5 nm (Desbois et al., 2009).

191 After polishing, the BIB cross-sections were coated with tungsten and imaged with a Zeiss Supra 55 SEM with
192 SE2, BSE, and EDX detector (Figure S3 in Supplementary data). SE2 images were used to image porosity and
193 BSE images are combined with an EDX map as well as EDX point analysis for identifying mineral phases. For
194 each cross-section, we made mosaics of hundreds of SE2 and BSE images at a magnification of 20,000x (~14.3
195 nm pixel value) and 10,000x respectively, with an overlap of 20% to 30%, (Klaver et al., 2012; 2015; 2016; Hemes
196 et al., 2013; 2015; 2016; Laurich et al., 2014). The mosaics are stitched together using Aztec software preserving
197 the original pixel resolution. Finally, these stitched images are used for the segmentation of pore spaces, minerals,
198 and other respective analyses.

199 Image segmentation and pore analysis

200 For quantifying porosity and pore morphology, individual SE2 image mosaics were segmented using a ‘seed and
201 grow’ algorithm (Adams and Bischof, 1994) implemented with a MatLab code (Jiang et al., 2015; Schmatz et al.,
202 2017) (Figure S3 in Supplementary data). The ‘seed and grow’ algorithm works based on the difference in intensity
203 of greyscale value in an image (bright = minerals, dark= pores). After automatic segmentation, individual pores in
204 SE2 images are manually corrected if required.

205 Similarly, using ImageJ software (threshold toolbox and machine learning algorithm), segmentation of the
206 individual mineral phases was carried out combining BSE images and EDX elemental maps. While quartz, calcite,
207 pyrite, mica minerals are efficiently segmented using these tools, feldspars are found difficult to segment because
208 of similar composition as clay (Figure S4, S5 and S6 in Supplementary data). Finally, corrected pore segmented

209 SE2 mosaics are overlaid on the phase maps using the ‘georeference’ tool of QGIS (<http://qgis.osgeo.org>), (Figure
210 S4, S5 and S6 in Supplementary data).

211 Pore detection resolution (PPR) and representative area analysis (REA)

212 ‘Practical pore detection resolution’ (PPR) indicates the pore sizes above which one can assume to detect 100% of
213 the pores present in the SE2 mosaic (Klaver et al., 2012). In agreement with earlier results using this instrument
214 (Klaver et al., 2012; 2015; 2016; Hemes et al., 2013; 2015; 2016; Laurich et al., 2014), we found PPR of ~2000
215 nm² and ~8500 nm² for the magnification of 20,000x and 10,000x images, respectively, corresponding to 10 pixels.

216 After segmenting all minerals, representative elementary area analysis (REA) was performed using the box
217 counting technique on mineralogical phase maps (Kameda et al., 2006; Klaver et al., 2012). Similar steps are also
218 followed for determining a representative elementary area for SE2 images. The estimated REA values using SE2
219 and BSE mosaics for the analyzed 33 mudstone samples are documented in Table S2 in Supplementary data.

220 Porosity, pore morphology, pore size, and the statistical distribution of pores were obtained using image analysis
221 techniques on 2D images collected using BIB-SEM technique. Because pores are non-spherical 3D objects that
222 are cut perpendicular to the bedding plane to acquire a 2D image dataset, there may be random and systematic
223 errors when comparing 2D and 3D results. We plotted shipboard measured MAD (moisture and density) porosity
224 vs depth (Fig.2e) and also BIB-SEM porosity vs depth for the analyzed samples (Fig.3a), where MAD porosity
225 documents bulk porosity for the sample, and BIB-SEM porosity represents 2D cuts of the non-spherical 3D
226 pores/porosity. As there is a first-order correspondence between the two porosity measurements, we deduce that
227 porosity and pore size distributions obtained from 2D image analysis reflect the bulk rock porosity and 3D pore
228 size distribution of the samples. In addition, the estimated REA appears appropriate for minimizing systematic
229 errors in the bulk pore characteristics of the sample.

230

231 Ion polishing and SEM technique (second set of samples; BEG, UT Austin).

232 22 Samples (SN-34 to SN-55 in Table 1) were taken shipboard from the sample half of the still-wet core in small
233 plastic tubes (similar to the ones used for the sample set at Aachen) inserted into the core by manual pressure. The
234 tubes were removed from the core and sealed in plastic bags. In the laboratory at the BEG, sample bags were
235 opened, and the muds were allowed to dry slowly in the tubes over several weeks. No discernible shrinkage was
236 observed as the dried core pieces still fully filled the tubes. The tubes were carefully removed, and a small cube
237 (approximately 0.5 to 1 cm³) was cut using a sharp knife and small hand saws; an orientation mark was placed on
238 the cube to indicate the bedding direction. Bed-perpendicular surfaces were prepared by Ar-ion cross-section
239 polishing, using the Leica EM TIC020 triple ion beam miller and coated with Ir for imaging. Manual placement
240 of the cut cubes into the ion mill is not precise so the ion-polished surfaces have slight variation from perpendicular
241 to bedding. Pore imaging was performed on the FEI Nova NanoSEM 430 using the in-lens SE detector, a 30 μm
242 aperture, 15 KeV accelerating current, a working distance of around 5–6 mm, and an intermediate-range sample
243 current (spot size = 3mm, mid-range for the instrument). Randomly selected views (typically 3-6) of all samples

244 were collected at 6000x machine magnification; additional views illustrating pore types and pore/grain
245 relationships were made at 10,000x to 30,000x (machine magnification).

246

247 Results

248 Compaction strain derived from MAD-porosity data

249 During Expedition 362, mass and volume of mud samples were measured in both wet and dry states using a high
250 precision electronic mass balance and helium pycnometer (http://www-odp.tamu.edu/publications/tnotes/tn37/tn37_8.htm). Using the obtained mass and volume dataset for wet and dry conditions, bulk MAD (moisture and
251 density) porosities were calculated. Porosity values reported by McNeill et al. (2017b) and downloaded from IODP
252 databases serve as the basis for strain calculations.

254 Shipboard MAD porosity for mud samples exhibits a sharp reduction from 80% to 52% from the seafloor to 28
255 mbsf (Fig.2e). Deeper samples display a comparatively smaller reduction in porosity of approximately from 52%
256 to 30% over a depth range of 28 to 1500 mbsf (Fig.2e and f).

257 We calculated compaction strain following a method proposed by Nollet et al. (2005) and subsequently used by
258 Neagu et al. (2010) (Fig.2g and h), assuming 1D consolidation and no change in solid volume. The compaction
259 strain (ϵ_c) is then computed as:

$$260 \quad \epsilon_c = \frac{1-\phi_0}{1-\phi_1} \quad (\text{Eqn-1})$$

261 Here ϕ_0 = initial porosity, and ϕ_1 = final porosity. Samples from sites U1480 and U1481 show no evidence of
262 tectonic faults (McNeill et al., 2017a), supporting an assumption of 1D strain. We considered the initial porosity
263 ϕ_0 as the MAD porosity at 0.6 mbsf depth ($\phi_0 = 80\%$). Compaction strain following Eqn-1 (Table S2 in
264 Supplementary data), is plotted against depth in Fig.2g and h. Compaction strain increases from 1 to 2.05 from the
265 seafloor to 28 mbsf (i.e. Unit I), and from 2.00 to 3.05 from 28mbsf to 1500 mbsf (Fig. 2g and h).

266 Another common measure of compaction is the intergranular volume (IGV; Paxton et al., 2002), which
267 corresponds to the sum of intergranular porosity and intergranular cement. In some mudstones, it may be necessary
268 to calculate IGV differently because of the presence of abundant primary intragranular pores and pore-filling
269 bitumen (Milliken and Olson, 2017). In our sample set, cement is absent, and IGV is taken to equal the bulk
270 porosity from shipboard MAD measurements.

271 Compactional porosity loss (COPL), referenced against the original sediment volume, is calculated from the initial
272 primary intergranular porosity (P_i ; 80% in this case) and the IGV as follows (Ehrenberg, 1989, Lundegard, 1992;):

$$273 \quad \text{COPL} = P_i - (((100 - P_i) \times \text{IGV}) / (100 - \text{IGV})) \quad (\text{Eqn-2})$$

274 At an IGV of 50%, COPL is 60%; in the deepest samples in the Nicobar fan (IGV of around 30%) COPL is 70%
275 (Table S2 in Supplementary data).

276 Description of grain microstructure and pore morphology

277 To have consistency in the data set, we prepared SE2 mosaics for all samples from the Aachen sample set at
278 20,000x magnification covering an average 100×100 μm² area. In addition, to examine the effect of magnification
279 on BIB-SEM porosity and representative area analysis (REA), three samples (i.e. SN-7, SN-15, and SN-29) were
280 also imaged each at 5,000x and 10,000x magnification, respectively. A decrease in magnification and resolution
281 reduces visible BIB-SEM porosity.

282 We observed consistent results for the REA analysis. For SE2 mosaics, REA varies between 45×45 μm² to 85×85
283 μm² at 20,000x magnification, and for segmented phase maps, REA varies between 90×90 μm² to 130×130 μm²
284 at 10,000x magnification. In the UT sample set, the standard images taken at 6000x with machine magnification
285 are 49.7×45.7 μm², so these images are also within the estimated REA range.

286 Based on EDX elemental map or point analysis, six mineral phases occur in significant amounts in the Sumatra
287 samples: quartz, feldspar (K-feldspar, Na-feldspar), calcite, pyrite, micas (muscovite, biotite, and chlorite), and
288 clay. Based on XRD analyses (Rosenberger et al., 2020), the clay size fraction is dominated by illite. Clay + mica
289 percentage in these mudstone samples varies between 65% to 75%. Samples SN-1 (77%) and SN-4 (76%) have
290 more clay + mica, whereas SN-7, SN-9, SN-17, SN-28, SN-29, and SN-31 contain less clay + mica (<65%) (Table
291 S2 in Supplementary data). It should be noted that, using EDX analysis, we are able to differentiate Na-feldspar,
292 and K-feldspar considering the concentration of Na and K elements in the grains. However, the XRD dataset
293 provides only information about the overall percentage of plagioclase feldspar present in these samples (Table 1),
294 perhaps an artifact of different detection limits for EDX and XRD analyses.

295 Using BIB-SEM and automatic pore segmentation techniques, an average of >30,000 pores have been detected
296 for each individual sample in the Aachen sample set at 20,000x magnification. Correlating with the MAD data set,
297 the estimated BIB-SEM porosity reduces from 32% to 19% over a depth range of seafloor to 28 mbsf, while the
298 deeper samples display a smaller reduction from 19% to 10% over a depth range of 28 to 1500 mbsf respectively
299 (Fig.3a). Consistent with numerous previous studies, the results document a mismatch between bulk measured
300 porosity (MAD) and imaging porosity (BIB-SEM) (e.g., Hemes et al., 2013; Houben et al., 2014; Nole et al., 2016;
301 Oelker et al., 2019) (Table S2 in Supplementary data). We plotted BIB-SEM porosity vs MAD porosity and found
302 an approximately linear correlation with coefficient of determination ($R^2 = 0.8621$) (Fig. 3b). It should also be
303 noted that, although there is a correlation, there is a large difference in the porosity values which increases with
304 increasing porosity.

305 Type of pores

306 Intergranular pores contribute >99% of the total visible porosity. Intragranular pores (see below) are rare. The size
307 and shape of intergranular pores change during compaction (Table S3 in Supplementary data).

308 Intergranular pores are classified (Fig.4) based on the size of surrounding particles (irrespective of mineralogy):
309 1) Clay domain (matrix) pores, and 2) silt-adjacent pores. Based on the variation in size, clay domain pores are
310 divided further into: 1) Large clay domain pores (pore size $>5 \times 10^5 \text{ nm}^2$) and the pore boundary is defined by more
311 than three clay particles; and 2) small clay domain pores (pore size $<5 \times 10^5 \text{ nm}^2$) that occur between 2-3 clay
312 particles (see further details below). Large and small clay domain pores are classified by geometry as: 1) Elongate
313 pores (aspect ratio $>3:1$) and 2) equant-shaped pores (aspect ratio $<3:1$). Elongate pores consist of 1) Linear-
314 elongated pores, and 2) crescent-shaped elongated pores. Examples of different clay-domain pore types are shown
315 in Fig. 5, 6, and 7.

316 Silt-adjacent pores are categorized by two types: 1) large silt-adjacent pores are $>5 \times 10^5 \text{ nm}^2$, and pore boundaries
317 are defined by more than three particles; and 2) small silt-adjacent pores include pore sizes $<5 \times 10^5 \text{ nm}^2$, and pore
318 boundaries are defined by two/three particles (see further detail on the modal sizes of these pore types below).
319 Large and small silt-adjacent pores are either: 1) Equant shaped (aspect ratio $<3:1$) or 2) elongated (aspect ratio
320 $>3:1$). Further, elongated silt-adjacent pores consist of 1) linear-shaped elongated pores and 2) crescent-shaped
321 elongated pores. These pore types are highlighted in Fig. 5, 6, and 7.

322 Change in inter-particle pore morphology with depth

323 *Seafloor to 28mbsf (Unit I)*

324 The shallow mud samples in Unit I are unconsolidated and porous (Fig. 5a). We analyzed a total of 10 samples (6
325 samples at Aachen and 4 samples at UT Austin) from this depth range. Among them, two samples have been
326 analysed both in Aachen as well as in Austin, respectively. Sample SN-1 (1.24 mbsf) has a maximum MAD
327 porosity of 80%. We observe three types of clay particle contacts in the microstructure of SN-1; edge to edge (EE),
328 edge to face (EF), and face to face (FF) contacts (Table S4 in Supplementary data). Among them, EF and FF
329 contacts are abundant and EE contacts are rare. The sample exhibits abundant large clay domain pores and large
330 silt-adjacent pores that are equant with smooth edges and a rounded pore perimeter. The sample also contains
331 abundant linear-elongated and equant-shaped small clay-domain pores. Crescent-shaped small clay domain pores
332 are rare in the microstructure of this sample. Equant-shaped, small silt-adjacent pores are abundant. In addition,
333 linear elongated and crescent-shaped small, silt-adjacent pores are also common (Fig.5a; Table S3 in
334 Supplementary data).

335 With increasing compaction strain ($\epsilon_c = 1.119$) and depth (5.1 mbsf; Figure S7 in Supplementary data), porosity
336 (MAD) reduces to 75% and corresponding COPL=19% (sample SN-2; Fig. 5b, Table S2 in Supplementary data).
337 The microstructures of SN-2 display are similar characteristics to those observed in sample SN-1, although there
338 are fewer large clay domain pores in SN-2 than SN-1. Linear elongated and equant-shaped small clay domain
339 pores are common (Table S3 in Supplementary data), but crescent-shaped small clay domain pores are rare. The
340 microstructures of SN-2 exhibit abundant equant-shaped large and small silt-adjacent pores.

341 With an increase in compaction strain to $\epsilon_c \sim 2.00$ (28 mbsf), the sample microstructure is dominated by FF contacts
342 (Fig. 5e), and EE and EF contacts are rare (Table S4 in Supplementary data). Additionally, large clay-domain
343 pores become infrequent in the microstructure (Fig.5e and Fig. 8). Crescent-shaped, small clay domain pores in

344 the microstructure are rare, whereas equant-shaped small clay domain pores are common. Both small and large
345 silt-adjacent pores exhibit equant shapes (Fig. 5e and Fig. 8d, e, f). The sample analyzed at the base of Unit I (SN-
346 6; 28 mbsf) contains rare large clay-domain pores and abundant FF contacts (Fig. 5c; MAD porosity = 54% and
347 COPL = 55%).

348 *28 mbsf to 1500 mbsf (Units II and III)*

349 Mud samples from the Nicobar fan section are more compacted than shallower samples (Fig. 6, 7 and Figure S8
350 in Supplementary data). We analyzed a total of 29 samples using at Aachen and 18 samples at UT Austin from
351 this section. An increase in compactional strain from 2.00 to 3.15 over a depth range of 28 to 1500 mbsf causes a
352 porosity reduction (MAD) of 54% to 28%, and the corresponding change in average COPL is 55% to 72%. The
353 microstructure of these samples is dominated by FF contacts among clay particles; EF and EE contacts are rare
354 (Table S4 in Supplementary data; Fig. 6 and 7 b, c). All samples exhibit abundant small linear-elongated clay
355 domain pores between two parallel clay sheets (Fig. 8b). Equant-shaped small, clay domain pores are rarely
356 observed below 150 mbsf depth ($\epsilon_c > 2.4$). Crescent-shaped, small, clay domain pores are rare at shallow depth but
357 become abundant with an increase in compactional strain $\epsilon_c > 2.95$ (871.87 mbsf) as the surrounding clay particles
358 are bent (Fig. 6). In addition, large clay domain pores in these samples are rarely observed in the vicinity of silt
359 clasts (Fig. 6).

360 Below 100 mbsf ($\epsilon_c = 2.20$), silt-adjacent small pores are dominantly equant shaped, but below 300 mbsf ($\epsilon_c > 2.5$)
361 silt-adjacent small pores are dominantly linear-elongated (Fig. 8e). Crescent-shaped, small, silt-adjacent pores are
362 common in all samples. Large silt-adjacent pores are dominantly equant above 200 mbsf depth ($\epsilon_c < 2.40$) and
363 commonly linear-elongate below 400 mbsf depth ($\epsilon_c > 2.5$) (Fig. 8f). It appears that due to an increase in
364 compactional strain, the shape of the silt-adjacent pores changes from equant to linear-elongated (Table S3 in
365 Supplementary data). In samples with more silt, equant-shaped small and large, silt-adjacent pores can persist at
366 greater depths (Fig. 8e and f).

367 Below 28 mbsf ($\epsilon_c > 2.0$), the number of large silt-adjacent pores in the microstructures decreases. Comparing
368 samples SN-8 (74.07 mbsf and $\epsilon_c = 2.09$) and SN-33 (1299.14 mbsf and $\epsilon_c = 2.51$) illustrates how the number of
369 large, silt-adjacent pores decreases with depth (Fig. 6a, and c) when the clay fraction (Table S2 in Supplementary
370 data) is comparable. This relationship is apparent even in samples separated by a smaller depth difference (SN-
371 49 from 959.14 mbsf and SN-55 from 1433.36 mbsf; Fig. 7b and c). While the number of large pores diminishes,
372 the maximum size of the large silt-adjacent pores remains constant (10^7 nm^2 ; Figure S9).

373 It can be observed in Fig. 2e that, around 1300 mbsf depth MAD porosity for the sample sets again rapidly
374 increases. However, microstructural observations of the sample from this horizon does not exhibit increase in
375 porosity (Fig. 6c). Hence, the increase in MAD porosity in this horizon is attributed to the increase in smectite
376 content (Fig. 2a) (Duttilleul et al., 2021). In general, the moisture and density method (MAD) overestimate the
377 measured porosity of the smectite rich sediment because of the inclusion of the interlayer water from smectite
378 during measurement (Brown and Ransom, 1996; Duttilleul et al., 2020).

379 Variation in the orientation of pores and grains due to compactional strain

380 We examined the change in orientation of the long axis of pores with increasing compaction strain. For all
381 segmented pores, the angle between the long axis and the bedding plane was determined and plotted in rose
382 diagrams (Supplementary data-15). Samples from the seafloor to 28 mbsf exhibit a weak preferred orientation of
383 the long axis of pores with maxima oriented obliquely to the bedding planes. However, below 28 mbsf the samples
384 have a preferred orientation of the long axis of pores aligned subparallel to the bedding plane. Further, due to an
385 increase in vertical effective stress down section below 28 mbsf in Units II and III, the degree of preferred
386 alignment of the long axis of pores only increases **by** a small amount (Figure S10).

387 We determined the angle between the long axis of individual silt grains and the bedding plane for all samples and
388 plotted the angle in a rose diagram (Figure S10). For quartz, feldspar, and calcite the degree of preferred orientation
389 of the long axis of grains changes little with depth. However, the rose diagrams obtained for mica show weak
390 maxima parallel to the bedding plane and several submaxima oriented obliquely to the bedding plane above 28
391 mbsf. Preferred alignment of the long axis of mica grains increases at 28 mbsf with a strong maximum oriented
392 parallel to bedding plane. Below 28 mbsf, further increase in the degree of preferred alignment is small.

393 Size distribution of pores

394 Pore size distributions (Fig. 9) of shallow samples (Unit I) are trimodal. Sample SN-1 has peaks between 10^5 to
395 10^6 nm², 10^6 to 10^7 nm², and 10^7 to 10^8 nm², and SN-2 has peaks from 10^4 to 10^5 nm², 10^5 to 10^6 nm², and 10^6 to
396 10^7 nm². These three pore size regimes correspond to the small clay domain and silt-adjacent pores, large clay
397 domain pores, and large silt-adjacent pores. Samples of Units II and III exhibit bimodal pore size distributions
398 (SN-10, SN-26, and SN-33 in Fig. 9). SN-10 has a peak between 10^5 to 10^6 nm², corresponding to small clay
399 domain and silt-adjacent pores, and 10^6 to 10^7 nm², reflecting large silt-adjacent pores. Large clay domain pores
400 are absent from samples below 28 mbsf depth (Units II and III) based on the pore size distributions combined with
401 image analysis. At shallow depths, the contribution to total porosity by larger silt-adjacent pores is greater
402 compared to the contribution by small clay domain pores (Fig. 9e and g). The contribution of large, silt-adjacent
403 pores to total porosity diminishes with depth. Hence, at greater depth, contribution to total porosity by larger silt
404 adjacent pore is less compared to small clay domain pores (Fig. 9i).

405 Pore size distributions follow a power-law shown on a double logarithmic graph following the equations (Klaver
406 et al., 2012; 2015; 2016; Hemes et al., 2013; 2015; 2016; Laurich et al., 2014):

$$407 \frac{N_i}{b_i S_{mosaic}} = C S_{pore}^D \quad (\text{Eqn-3})$$

$$408 \log\left(\frac{N_i}{b_i S_{mosaic}}\right) = -D \cdot \log(S_{pore}) + \text{Log } C \quad (\text{Eqn-4})$$

409 Where N_i = number of pores with area S_{pore} , b_i = bin size, S_{mosaic} = surface area of the current mosaic, C =constant,
410 and D = power-law exponent. The resulting power-law exponent (D) varies between 1.70 to 2.00 (Table T2 in
411 Supplementary data).

412 Effect of texture on porosity, pore morphology, and orientation of pores

413 We analyzed six samples (SN-7, SN-9, SN-17, SN-28, SN-29, and SN-31) that are enriched in silt content
414 compared to the rest of the mud samples (Table T2 in Supplementary data)). Silt content has a positive correlation
415 to the total SEM porosity. For example, sample SN-29 (1172.88 mbsf) exhibits a BIB-SEM porosity of 14%
416 whereas other samples from a similar depth with less silt exhibit an average BIB-SEM porosity of 12% (Table T2
417 in Supplementary data)) at 20000x magnification. The samples with greater silt content are also enriched in equant-
418 shaped silt-adjacent larger pores (Fig.10a). We also estimated the orientation of the long axis of pores for these
419 three samples and plotted the obtained results as rose diagrams (Fig.10b). The obtained results exhibit a relatively
420 weak preferred alignment of the long axis of pores with respect to the bedding planes (Fig.10b).

421

422 Discussions

423 Effective stress vs porosity: A comparison with experimental study

424 To understand the consolidation mechanisms of the Sumatra sediments, we estimated vertical effective stress
425 following the steps proposed by Hüpers et al. (2015). Following Terzaghi and Peck (1948), vertical effective stress
426 (σ_v') is expressed as:

$$427 \sigma_v' = \sigma_v - P_f \quad (\text{Eqn-5})$$

428 Here σ_v = total vertical stress caused by the overburden load, and P_f = fluid pressure. To compute vertical effective
429 stress of a layered sediment, we use Eqn 6:

$$430 \sigma_v' = \sum(\rho_s - \rho_w) \cdot g \cdot \Delta z \quad (\text{Eqn-6})$$

431 where ρ_s = bulk density of the sediment, ρ_w = density of the pore water, Δz = depth interval, and g = gravitational
432 acceleration. Although small offset strike-slip faults are evident at the seafloor and in seismic reflection profiles
433 (McNeill et al., 2017a), the amount of strain attributed to these fault offsets supports the idea that the maximum
434 horizontal stress is comparable to the vertical stress; there is no evidence in seismic reflection data or from core
435 microstructures for thrust or reverse faults associated with a vertical least principal stress. On this basis, we assume
436 that vertical stress is the maximum principal stress, and that pore pressure is hydrostatic. Bulk density of the
437 sediment ρ_s was acquired from MAD data set obtained from IODP website (McNeill et al., 2017a), and ρ_w was
438 considered as the density of seawater i.e. 1025 kg/m³ (Hüpers et al., 2015).

439 We plotted vertical effective stress against MAD porosity for 55 mud samples (Fig.11). Fawad et al. (2010)
440 experimentally studied the consolidation behavior of mud with varied proportions of silt and clay. While Sumatra
441 samples follow trends like those defined by Fawad et al. (2010), the experimental samples are more compacted
442 than natural Sumatra samples for the same silt content.

443 Clay mineralogy has a significant effect on the compaction behavior of mudstone (Mondol et al., 2007). Mondol
444 et al. (2007) performed compaction experiments using pure smectite and pure kaolinite clay particle packs because
445 they represent two end members compared to other clay minerals (illite and chlorite) in terms of grain size and
446 surface area. Smectite is the more fine-grained clay with the largest surface area while kaolinite is coarser and has
447 a smaller surface area than other clay mineral types (Meade, 1964; Mesri and Olson, 1971; Rieke and Chilingarian,
448 1974). Kaolinite is more compressible than smectite, and clay compaction gradually decreases with increasing the
449 proportion of small size clay particles in the sample (Mondol et al, 2007).

450 Fawad et al., (2010) used clay mixtures of 81% kaolinite, 14% mica, and 5% microcline grains, whereas Sumatra
451 mud samples are composed of 50%-79% illite and 5%-30% smectite, with only 8-20% undifferentiated chlorite
452 and kaolinite and 5-10% quartz particles. Therefore, due to higher illite and smectite content, Sumatra muds
453 appeared to be less compacted than the experimental samples used by Fawad et al. (2010).

454 BIB-SEM porosity vs MAD porosity

455 We note that BIB-SEM porosity is lower than the porosity found from shipboard MAD data, however the two
456 measurements correlate along a line through the origin. (Fig.3b). The reason for this difference is that MAD
457 porosity measures the total amount of moisture in a much larger sample and accounts for pores much below the
458 PPR. Rare large pores are also under-represented in the 1 mm² BIB section. Earlier studies also documented and
459 discussed mismatches between MAD and BIB-SEM measurements (Hemes et al., 2013; Houben et al., 2014; Nole
460 et al., 2016; Oelker et al., 2019). They concluded that the mismatch could be due to several factors; i) BIB-SEM
461 porosity largely depends on the magnification and resolution of images, ii) variation in sample sizes, and iii) MAD
462 porosity takes into account the pores whose sizes are much lower than PPR, whereas BIB-SEM technique detects
463 only the pores larger than PPR. We plotted estimated BIB-SEM porosity and MAD porosity data from earlier
464 studies on Boom clay (Hemes et al., 2013; Oelker et al., 2019); Opalinus clay (Houben et al., 2014) and samples
465 from the Nankai trough (Nole et al., 2016). The data for Boom clay and Opalinus clay follow a similar trend to the
466 Sumatra samples, whereas clay samples from the Nankai trough shows a different trend. This difference may be
467 attributed to differences in magnification of Nankai trough samples.

468 In addition, we plotted clay content against the difference between the two porosities in Fig.12a. We performed
469 regression analysis using the data set for the 33 mud samples analyzed at Aachen (Fig.12b) for BIB-SEM porosity
470 versus MAD porosity (following Eqn-7) but also incorporating the effect of clay content (following the Eqn-8).

$$471 \text{ BIB-SEM porosity} = a * \text{MAD porosity} + c \quad (\text{Eqn-7})$$

$$472 \text{ BIB-SEM porosity} = a * \text{MAD porosity} + b * \text{clay content} + c \quad (\text{Eqn-8})$$

473 The coefficient of determinations (R^2) for Eqn-7 and Eqn-8 are 0.7126 and 0.9262 respectively. These results
474 suggest that the ratio in porosity depends on depth and clay content.

475 For all samples, the BIB-SEM pore size distribution follows a power-law over an interval of three orders of
476 magnitude. We may extrapolate this below the practical pore resolution (PPR; Klaver et al., 2012; Kuila and

477 Prasad, 2013; Wang et al., 2019). Extrapolating our data set down to 3 nm pore diameter, the BIB-SEM porosity
478 increases only up to 20%~25%. A mismatch of 15% to 20% between the MAD porosity and extrapolated BIB-
479 SEM porosity remains. The fall -off from the normal trend in log-log pore size distribution plots (Fig.9b) for the
480 shallow depth (Unit-I) samples suggest that also large pores are also under-counted in the data set. The mud
481 samples from Unit-I contains forams that are rare or absent in the deeper section (Figure S11 a, b, c, and d in
482 Supplementary data), and part of missing pore volume can be attributed to the intact forams that may be missed
483 due to the small size of the BIB SEM sample.

484 Another factor that can create a mismatch between data sets is drying artefacts. In the past, Desbois et al. (2014)
485 performed a detailed study on drying artefacts of mudstone samples using Cryogenic BIB-SEM technique. They
486 identified four types of drying damages (Type-I, II, III and IV) that can develop during drying of a mudstone.
487 Type-I and type-II drying damage develops at clay/clay particle interfaces with tip to long axis contact, and at
488 clay/clast interfaces. Heterogeneous deformational behavior or shrinkage strain of clay and/or non-clay mineral
489 grains can cause a build-up in stress at the boundary between particles during drying. Type-III drying artefacts are
490 large cracks that develops within the clay matrix itself. Type-IV drying artefacts are the small damages that modify
491 pore morphology during drying. Among all of them, Type-II and III are the most spectacular and large enough to
492 modify microstructure significantly. The morphology of the type-II and III drying artefacts are characterized by
493 large irregular shaped very elongated pores with serrated pore boundaries. However, in the present study, the large
494 clay domains and silt-adjacent pores in all samples potentially show smooth edges and rounded pore tip-end, which
495 are incompatible with the typical morphologies of the drying artefacts (Fig. 5, 6 and 7). Hence, drying artefacts
496 appear to be less important for reconciling a mismatch between MAD and BIB-SEM porosity.

497 Shallow samples from Unit-I are richer in smectite content than deeper samples, although a few samples from 400
498 to 1000 mbsf have similar smectite abundances as Unit I. The moisture and density method (MAD) may
499 overestimate the measured porosity of the sediment if interlayer water from smectite is included in the
500 measurement (Brown and Ransom, 1996; Dutilleul et al., 2020). Greater smectite content in the shallow samples
501 (Unit-I) may have contributed to an overestimation of the MAD porosity in the study. This is also consistent with
502 the observation that the difference between the measurements getting larger as porosity increases.

503 Micromechanical model for porosity reduction

504 Sharp reduction in porosity at the shallow depth from the seafloor to 28 mbsf

505 High porosity (80% MAD; 32% BIB-SEM) in the shallowest sediments is attributed to large pores in the samples
506 created by abundant EE and EF particle contacts (Fig. 5a and 7a). These contacts are unstable and collapse under
507 low effective stress to form FF contacts, resulting in a rapid porosity decrease within the first 28m of burial
508 (Supplementary data-11). This deformation is apparent from the reduction of large clay domain pores observed
509 over this interval (Fig. 8; Supplementary data-10). Collapse of pores surrounded by EE and EF contacts is further
510 recognized by the progressive alignment of clay particles into the bedding plane, which promotes an increase in
511 the number of elongated, small, clay domain pores parallel to the bedding plane. Each of these observations is
512 consistent with rotation of clay particles into the bedding plane as these large clay-domain pores collapse.

513 Mechanism of porosity reduction from 28 mbsf to 1500 mbsf

514 Below 28 mbsf to >1500 mbsf, porosity continues to decrease from 52-30% (MAD) but at a reduced pace. SEM
515 observations suggest that this porosity decline results from the progressive loss of silt-adjacent pores with large
516 silt-adjacent pores lost before small ones (Fig. 8), although they remain present in common abundance to 1200
517 mbsf. Small clay domain pores are abundant throughout the section, and the large clay domain pores are lost
518 **between the seafloor and** 28 mbsf.

519 Within the population of silt-adjacent pores, the large, equant pores are most susceptible to collapse (Fig. 8). Large,
520 elongate pores persist in abundance, both in linear and crescent geometries. While it seems plausible that large,
521 equant pores collapse to form large, elongate pores, no corresponding increase in the elongate pore population is
522 observed. Large, elongate pores may collapse further and become small silt-adjacent pores. Microstructural
523 evidence supports the idea that large equant pores collapse as surrounding clay particles within clay-rich domains
524 bend and shrink the size of the remaining pore (Fig.13), and that the collapse results in an increasing aspect ratio
525 of the pore.

526 Frequently, bent clay particles are observed on the top of larger silt-adjacent pores. In the clay microstructure,
527 large silt-adjacent pores act as a zone of heterogeneous strain localization. Clay particles can bend and collapse
528 into large silt-adjacent pores more readily than the smaller pores in the clay matrix (Fig.13a to f). With increasing
529 vertical effective stress two situations can arise which are demonstrated in the model shown in Fig.13g. First, with
530 an increase in effective stress, the bent clay particles can lose frictional resistance from the sidewall (Fig.13a and
531 b), can continue to bend, and slide down to fill the larger silt-adjacent pore space (Fig.13g-(iii)). Second, with an
532 increase in vertical effective stress, bent clay particles may develop fractures (red lines in Fig.13g-(iv)) and
533 subsequently collapse into the larger silt-adjacent pore space to reduce the porosity of samples (Fig.13g-(v)).
534 Fig.13a represents fractured bent clay on the top of the larger silt adjacent pore (shown by white arrow). Similarly,
535 two small clay particles appear to have fallen into the larger silt adjacent pore space (Fig.13e) while another bent
536 clay particle (shown by white arrow) covers the pore. Fig.13f represents a bent clay particle wrapping across the
537 top of two quartz particles, and four small clay platelets fill the space between two quartz particles, suggesting an
538 older, larger silt-adjacent pore filled by fractured clay platelets. Occurring within the pore space between two
539 equant quartz grains (Fig.13f), four small clay particles appear to have developed due to the fracturing of two large
540 bent clay particles. Hence, it appears that the collapse of larger silt-adjacent pores in these mud samples is governed
541 by the bending of clay particles and subsequent fracturing due to an increase in vertical effective stress. While
542 these processes are defined within individual pores, the observed deformation is interpreted to result from an
543 imposed force chain that acts on specific pores in a progressive manner as the force chain evolves and as adjacent
544 pores deform.

545 Small silt-adjacent pores also become less abundant with burial, but the transition occurs deeper than the large
546 pores, and small, silt-adjacent pores remain common throughout the section (Fig. 8; Supplementary data-11).
547 Small equant pores are lost like the large pores, and elongate pores remain abundant within this population subset
548 throughout. There is a loose correspondence between the loss of small, equant pores and an increase in elongate

549 pores, suggesting that pore flattening is part of the pore collapse history. The pore collapse evolution outlined for
550 large pores (Fig.13g) appears to also hold for small pores, even though observations are more challenging.

551 Small, clay domain pores appear to remain resilient throughout the compaction history (Fig. 8), even though some
552 of these pores must become lost to account for porosity loss. Small, equant pores are lost between 100-200 m, and
553 this loss appears to be accommodated by an increase in elongate pores (Fig. 8). Elongate crescent pores increase
554 in abundance around 800 mbsf, and we interpret this to reflect folding of abundant linear elongate pores as the
555 overall system compacts.

556 Large equant pores in the clay domain are lost within the first few 10's of meters of burial. Elongate pores appear
557 to form at the expense of equant pores, and there may be a reduction in pore size associated with this shape change.
558 Most of the pores remaining after 1500 m of burial are small, elongate pores found both in clay domain and silt-
559 adjacent pores.

560 The presence of silt particles locally redistributes the force chain of load to retain undeformed, silt-adjacent, large
561 pores (Schneider et al., 2011). The samples with greater silt content are also enriched in equant-shaped silt-adjacent
562 larger pores (Fig.10) in the microstructure. Hence, as a result, they display greater porosity compared to other
563 samples from similar depth intervals (Fig.10).

564 Previous studies report contrasting ideas on the development of phyllosilicate fabric strength due to mechanical
565 compaction. Some studies suggest that mechanical compaction creates a phyllosilicate fabric in mud (Bowles et
566 al., 1969; Oertel and Curtis, 1972; Vasseur et al., 1995), whereas other studies conclude that vertical effective
567 stress has limited impact on phyllosilicate fabric development (Ho et al., 1999; Aplin et al., 2006; Day-Stirrat et
568 al., 2008; 2011). Here, we consider the preferred orientation of pores as a proxy for the alignment of phyllosilicate
569 (Hemes et al., 2013). At shallow depth (Unit-I), a weak preferred alignment of the long axis of pores with maxima
570 oriented obliquely to the bedding planes is formed (Supplementary data-15), and at greater depth (Unit-II and III)
571 the long axes of pores become aligned subparallel to the bedding plane. Increase in vertical effective stress below
572 28 mbsf depth creates only a small increase in the preferred orientation of the long axis of pores. Hence, we found
573 only a limited change in phyllosilicate fabric strength with increasing vertical stress..

574 Previous authors also document the evolution of pore size **distribution** in mud with an increase in consolidation
575 stress using laboratory experiments and mercury-intrusion porosimetry (Griffiths and Joshi, 1989; 1990). They
576 conclude that the pore size distribution appears to be bi-modal, and the distribution curve shifts toward smaller
577 pore sizes with an increase in applied consolidation stress (Griffiths and Joshi, 1989). We observe an initial
578 transition from tri-modal to bi-modal pore size distribution around 28 mbsf depth due to rapid collapse of large
579 clay domain pores by compactional strain. With an increase in depth below 28 mbsf, the bi-modal pore size
580 distribution persists and tends to shift toward small pore sizes as the number of larger silt-adjacent pores
581 diminishes.

582 Laboratory studies have emphasized the importance of clay particle rotation as a dominant mechanism for
583 mechanical compaction in mudstone (Bennett et al., 1981, 1991; Vasseur et al., 1995; Aplin et al., 2006; Day-
584 Stirrat et al., 2008; 2011). We observe particle rotation only in the shallowest samples where unstable EE and EF

585 particle contacts are present. Clay particle bending and sliding/fracturing are considered more important for most
586 of the section studied.

587 Mechanical compaction of marine sediment: a conceptual model

588 According to earlier studies (Delage and Lefebvre, 1984; Griffiths and Joshi, 1989; 1990; Emmanuel and Day-
589 Stirrat 2012), the reduction of pores in sedimentary rocks during compaction is size-dependent - larger pores
590 deform much readily than smaller pores. According to their model, larger pores rapidly decrease in size during
591 compaction to reduce the overall porosity of the sample. However, microstructural analysis of Sumatra samples
592 suggests that porosity reduction is accomplished by compaction of all pore sizes. Moreover, the maximum size of
593 pores remains almost constant irrespective of increasing vertical effective stress/depth (Supplementary data-8)
594 with little difference observed for the maximum pore size in samples from 98.25 mbsf and 1299.31 mbsf. The
595 preservation of a constant ratio between MAD and BIB-SEM porosity measurements (Fig. 3b) suggests that
596 porosity loss is distributed across all pore sizes. We infer that all pore sizes are available for compaction for every
597 increment of applied stress but acknowledge that pore size reduction in different size classes may proceed at
598 different rates.

599 We propose a new model for the reduction in porosity in which all pores within the force chain of load take part
600 in the reduction of porosity during compaction irrespective of their size. At shallow depth up to 28mbsf, larger
601 clay-domain pores are the most susceptible to early response during an increase in compactional strain, because of
602 two reasons: 1) the 'domains' defined by the clay particles are weaker compared to the larger, rigid silt grains, and
603 2) due to higher relative proportion of clay-rich regions within the mud, the force chain of load dominantly passes
604 through the clay domains. The dispersed nature of the silt-size particles and the high proportion of phyllosilicates
605 in the mud samples indicate that soft clay particles act as the principal load-bearing framework. Hence, larger clay
606 domain pores are more unstable compared to silt-adjacent pores in the mud microstructure. Similarly, below
607 28mbsf depth, under an increase in vertical effective stress, both the larger silt-adjacent pores and smaller pores in
608 the clay matrix that come within the force chain of load collapse. Hence, the ratio between BIB-SEM porosity vs
609 MAD porosity remains almost constant irrespective of the depth. All larger silt-adjacent pores do not come within
610 the force chain of load at the same time. Hence, some of the larger silt-adjacent pores remained undeformed to the
611 maximum depth of 1500mbsf depth. Therefore, the maximum size of the larger silt-adjacent pores remains almost
612 constant irrespective of the depth/vertical effective stress.

613 In this study, we investigated how systematically pore types evolve with increasing depth in naturally compacted
614 samples. However, tracking the pore evolution through additional size categories would elucidate the pore
615 evolution in more detail. Preliminary pore size distribution data (Fig.9) indicate that 4 size bins exist in these
616 samples. Developing this approach requires improved image analysis techniques to tie all the pore attributes
617 together on a pore-by-pore basis for a huge number of pores.

618 Compaction strain accommodation and grain-scale deformation

619 Deformation of clay-rich sedimentary rocks involves four possible mechanisms: 1) Particulate flow; (Morgenstern
620 and Tchalenko, 1967; Borradaile et al., 1981); 2) Cataclasis; (Ukar and Cloos, 2019) 3) Diffusive mass transfer;

621 (Blenkinsop, 2007; Fossen, 2016); 4) Intercrystalline plasticity (Blenkinsop, 2007; Fossen, 2016). Intensity and
622 occurrence of a particular deformation mechanism in a mudstone depend on several parameters, such as effective
623 stress, water content, cementation, temperature (Desbois et al., 2017; Den Hartog and Spiers, 2014).

624 All our samples show evidence of particulate flow controlled by friction between grains. At shallow depths, illite
625 platelets contacted at EE and EF junctions lose these weak bonds, and particles rotate into bedding-parallel
626 orientation. Once FF contacts dominate, large-scale rotations are reduced, and **inter**-particle slip becomes
627 important. This is best evidenced in collapse of large, silt-adjacent pores where bent clay particles **overlay** pores
628 (Fig.14a to f). In deforming granular foam material, bending was reported as the dominant deformation mechanism
629 for the reduction in porosity and developing preferred alignment of the long axis of pores perpendicular to the
630 applied stress (Elliott et al., 2002, Zhou et al., 2004; Samsudin et al., 2017; Zakaria et al., 2018) (review of these
631 earlier studies on the experimental deformation of granular foam is described in document S2). Friction adheres
632 clay particles to the edge of pores while the middle of particles drops into the pore, resulting in bending by intra-
633 particle slip. A cartoon (Fig.14g) illustrates the compaction mechanism associated with the bending of clay
634 particles. With increasing compaction strain, clay particles undergo bending, and as a result, pore area reduces,
635 and the orientation of the pores tends to align perpendicular to the applied effective stress (Fig.14g). At shallow
636 depths (Unit-I), particles get enough free space for rotation to align parallel to the bedding plane because of higher
637 porosity (Figure S12a and b). However, at greater depth where porosity decreases, space problems limit particle
638 deformation to bending and fracturing as increase in compactional strain increases (Figure S12c and d).

639 [Compaction of Sumatra input section: generalized implication for rock property](#) 640 [evolution](#)

641 The overall compaction curve obtained for Sumatra muds is comparable with the experimental study by Fawad et
642 al., 2010 in the context of compactional range (Fig.8). The curve shows a mono-exponential decrease in porosity
643 with an increase in vertical effective stress, which is evidence of normal consolidation (Fawad et al., 2010;
644 Dutilleul et al., 2020).

645 The larger silt-adjacent pores seen in the deepest of these samples (1500 m burial) suggest these muds retain
646 considerable potential for additional mechanical compaction with deeper burial. As this marine sediment
647 progressively approaches greater burial closer to the accretionary prism, it will undergo further change in physical
648 and deformational properties (Bray and Karig, 1985). Despite the substantial compactional strain, the relatively
649 high porosity of the deepest sample and the survival of larger and mechanically unstable silt-margin pores suggests
650 that compactional stabilization has yet to be reached because such IGVs and pore types are not generally observed
651 in older and lithified mudrocks. Based on the current understanding of subduction zone deformation behavior and
652 mudrock properties, it seems likely that mechanical compaction will continue to dominate the pore loss in deeper
653 burial.

654 The general absence of early cementation and the corresponding dominance of **mechanical** compaction in the total
655 pore loss is consistent with observations of other siliciclastic-dominated muds (Milliken, 2014; 2019). The trends
656 for intergranular volume change observed from the seafloor and 1500 mbsf place useful constraints on the

657 maximum cement volumes that theoretically could be emplaced at this depth range in sediments containing a more
658 reactive grain assemblage. At the depths of burial attained at the deformation front, any cementation of the Sumatra
659 input sediments will be limited to <30% of the rock volume, or possibly much less, as mechanical compaction is
660 expected to continue up to the burial temperatures that initiate grain reactions and associated cementation.

661 Conclusions

662 Pores are classified by size and microstructural position, resulting in a multi-modal contribution to the total
663 porosity. Shallow samples (seafloor to 28 mbsf) display a sharp reduction in porosity from 80% to 52% as large
664 clay domain/matrix pores collapse. Deeper samples (28 mbsf to 1500 mbsf) exhibit a smaller reduction in porosity
665 from 50% to 32% due to the collapse of silt-adjacent pores by bending and subsequent fracturing/sliding of clay
666 particles.

667 The class of large pores next to silt-sized grains (between 10^4 and 10^6 nm²) remains common to >1 km burial,
668 irrespective of the mineralogy of the silt-sized grains, but their size decreases with depth. Small, equant pores next
669 to silt particles are abundant in the first 100 m of burial and remain common over the entire depth range.

670 Small pores in clay domains are almost all elongated, and abundant over all observed depths. Small, crescent-
671 shaped elongate pores increase in abundance with depth as clay particles become folded by compactional
672 processes.

673 The size-independence of pore loss arises because the force chain driving pore collapse is localized primarily
674 within the volumetrically dominant and weaker clay-rich domains; larger pores around isolated silt particles enter
675 into the force chain somewhat randomly and asynchronously and do not contribute preferentially to pore loss over
676 the depth range studied.

677 An increase in effective stress up to 18 MPa (~1500 mbsf) causes the development of weakly aligned phyllosilicate
678 fabric (defined by mica and illite clay particles) in the microstructure.

679 Compaction processes in our samples are dominated by granular flow (rotation and frictional sliding of illite clay
680 particles) at shallow depths. With increasing depth, compaction is additionally accommodated by bending of clay
681 particles.

682 Data availability

683 High resolution SE2 and BSE images of all samples are available online at:
684 <https://figshare.com/s/cbaada517b0b1409d575>

685 Authors contributions

686 SL and KLM performed sample preparation and BIB-SEM microscopy. SL analysed the data. JLU and GD
687 acquired funding. JLU managed the project. PV, KLM and JLU significantly contributed to interpret the data. SL

688 wrote the first draft of the manuscript. PV, KLM and JLU contributed for the correction and improvement of the
689 manuscript.

690 Competing interests

691 The authors declare that they do not have any conflict of interest.

692 Acknowledgments

693 SL and JLU thank German Research Foundation (Deutsche Forschungsgemeinschaft [DFG] grant UR 64/19-1)
694 for providing funding to carry out the research. IODP (International Ocean Discovery Programme) sample
695 repository, Japan is acknowledged for providing oriented mud samples for the study. KLM acknowledges the
696 samples and data provided by the International Ocean Discovery Program (IODP). Funding for sample preparation
697 and SEM imaging was supported by a post-expedition award (Milliken, P.I.) from the Consortium for Ocean
698 Leadership. SL thanks Manuel Menzel, Jop Klaver, Liene Spruženiece, and Joyce Schmatz for providing valuable
699 time to teach BIB-SEM techniques. We would like to thank Dave Dewhurst and Bernhard Schuck for their
700 constructive ideas in the review reports, and Virginia Toy for editorial handling.

701 References

702 Adams, R. and Bischof, L.: Seeded region growing. IEEE Transactions on pattern analysis and machine
703 intelligence. IEEE: 16(6), 641-647. [https://DOI. 10.1109/34.295913](https://doi.org/10.1109/34.295913), 1994.

704 Ajdukiewicz, J. M. and Lander, R. H.: Sandstone reservoir quality prediction: state of the art, AAPG Bulletin, 94, :
705 1082-1091, [https:// doi.org/10.1306/intro060110](https://doi.org/10.1306/intro060110), 2010.

706 Ammon, C.J., Ji, C., Thio, H.K., Robinson, D., Ni, S., Hjorleifsdottir, V., Kanamori, H., Lay, T., Das, S.,
707 Helmberger, D. and Ichinose, G. Rupture process of the 2004 Sumatra-Andaman earthquake, Science, 308(5725),
708 1133-1139, DOI: 10.1126/science.1112260, 2005.

709 Aplin, A.C. and Macquaker, J.H.: Mudstone diversity: Origin and implications for source, seal, and reservoir
710 properties in petroleum systems, AAPG bulletin, 95(12), 2031-2059, <https://doi.org/10.1306/03281110162>, 2011.

711 Aplin, A.C., Matenaar, I.F. and Vvan Dder Pluijm, B.A.: Influence of mechanical compaction and chemical
712 diagenesis on the microfabric and fluid flow properties of Gulf of Mexico mudstones Journal of Geochemical
713 Exploration, 78, 449-451, [https://doi.org/10.1016/S0375-6742\(03\)00035-9](https://doi.org/10.1016/S0375-6742(03)00035-9), 2003.

714 Aplin, A.C., Matenaar, I.F., McCarty, D.K. and Vvan Der Pluijm, B.A.: Influence of mechanical compaction and
715 clay mineral diagenesis on the microfabric and pore-scale properties of deep-water Gulf of Mexico mudstones,
716 Clays and Clay Minerals, 54(4), 500-514, <https://doi.org/10.1346/CCMN.2006.0540411>, 2006.

717 Backman, J., Chen, W., Kachovich, S., Mitchison, F. L., Petronotis, K. E., Yang, T. and Zhao, X.: Data report:
718 Revised age models for IODP Sites U1480 and U1481, Expedition 362, Proceedings of the International Ocean
719 Discovery Program, Expedition Reports 362, <https://doi.org/10.14379/iodp.proc.362.202.2019>, 2019.

720 Baruch, E.T., Kennedy, M.J., Löhr, S.C. and Dewhurst, D.N.: Feldspar dissolution-enhanced porosity in
721 Paleoproterozoic shale reservoir facies from the Barney Creek Formation (McArthur Basin, Australia). AAPG
722 Bulletin, 99(9), 1745-1770, <https://doi.org/10.1306/04061514181>, 2015.

723 Bennett, R.H., Bryant, W.R. and Keller, G.H.: Clay fabric of selected submarine sediments; fundamental properties
724 and models, Journal of Sedimentary Research, 51(1), 217-232, <https://doi.org/10.1306/212F7C52-2B24-11D7-8648000102C1865D>, 1981.

726 Bennett, R.H., O'Brien, N.R. and Hulbert, M.H.: Determinants of clay and shale microfabric signatures: processes
727 and mechanisms. In *Microstructure of Fine-Grained Sediments*, 5-32, Springer, New York, NY. https://DOI:10.1007/978-1-4612-4428-8_2, 1991.

729 Blenkinsop, T.G.: *Deformation microstructures and mechanisms in minerals and rocks*, Springer Science &
730 Business Media, 2007.

731 Bowles, F.A., Bryant, W.R. and Wallin, C.: Microstructure of unconsolidated and consolidated marine sediments,
732 Journal of Sedimentary Research, 39(4), 1546-1551, <https://doi.org/10.1306/74D71E7E-2B21-11D7-8648000102C1865D>, 1969.

734 Borradaile, G.J.: Particulate flow of rock and the formation of cleavage. *Tectonophysics*, 72(3-4), 305-321,
735 [https://doi.org/10.1016/0040-1951\(81\)90243-2](https://doi.org/10.1016/0040-1951(81)90243-2), 1981.

736 Bray, C.J. and Karig, D.E.: Porosity of sediments in accretionary prisms and some implications for dewatering
737 processes, Journal of Geophysical Research: Solid Earth, 90(B1), 768-778, <https://doi.org/10.1029/JB090iB01p00768>, 1985.

739 Brown, K.M. and Ransom, B.: Porosity corrections for smectite-rich sediments: Impact on studies of compaction,
740 fluid generation, and tectonic history. *Geology*, 24(9), 843-846, [https://doi.org/10.1130/0091-7613\(1996\)024<0843:PCFSRS>2.3.CO;2](https://doi.org/10.1130/0091-7613(1996)024<0843:PCFSRS>2.3.CO;2), 1996.

742 Burland, J.B.: On the compressibility and shear strength of natural clays. *Géotechnique*, 40(3), 329-378,
743 doi.org/10.1680/geot.1990.40.3.329, 1990.

744 Chester, F.M., Rowe, C., Ujiie, K., Kirkpatrick, J., Regalla, C., Remitti, F., Moore, J.C., Toy, V., Wolfson-
745 Schwehr, M., Bose, S. and Kameda, J.: Structure and composition of the plate-boundary slip zone for the 2011
746 Tohoku-Oki earthquake. *Science*, 342(6163), 1208-1211, <https://DOI:10.1126/science.1243719>, 2013.

747 Cetin, H.: Soil-particle and pore orientations during consolidation of cohesive soils. *Engineering geology*, 73(1-
748 2), 1-11, doi.org/10.1016/j.enggeo.2003.11.006, 2004.

749 Day-Stirrat, R.J., Aplin, A.C., Środoń, J. and Van der Pluijm, B.A.: Diagenetic reorientation of phyllosilicate
750 minerals in Paleogene mudstones of the Podhale Basin, southern Poland, *Clays and Clay Minerals*, 56(1), 100-
751 111, DOI: 10.1346/CCMN.2008.0560109, 2008.

752 Day-Stirrat, R.J., Flemings, P.B., You, Y., Aplin, A.C. and van der Pluijm, B.A.: The fabric of consolidation in
753 Gulf of Mexico mudstones, *Marine Geology*, 295, 77-85, <https://doi.org/10.1016/j.margeo.2011.12.003>, 2012.

754 Day-Stirrat, R.J., Milliken, K.L., Dutton, S.P., Loucks, R.G., Hillier, S., Aplin, A.C. and Schleicher, A.M.: Open-
755 system chemical behavior in deep Wilcox Group mudstones, Texas Gulf Coast, USA, *Marine and Petroleum*
756 *Geology*, 27(9), 1804-1818, <https://doi.org/10.1016/j.marpetgeo.2010.08.006>, 2010.

757 Day-Stirrat, R.J., Schleicher, A.M., Schneider, J., Flemings, P.B., Germaine, J.T. and van der Pluijm, B.A.:
758 Preferred orientation of phyllosilicates: Effects of composition and stress on resedimented mudstone
759 microfabrics, *Journal of Structural Geology*, 33(9), 1347-1358, <https://DOI:10.1016/j.jsg.2011.06.007>, 2011.

760 Dean, S.M., McNeill, L.C., Henstock, T.J., Bull, J.M., Gulick, S.P., Austin, J.A., Bangs, N.L., Djajadihardja, Y.S.
761 and Permana, H.: Contrasting décollement and prism properties over the Sumatra 2004–2005 earthquake rupture
762 boundary, *Science*, 329(5988), 207-210, <https://DOI: 10.1126/science.1189373>, 2010.

763 Delage, P. and Lefebvre, G.: Study of the structure of a sensitive Champlain clay and of its evolution during
764 consolidation. *Canadian Geotechnical Journal*, 21(1), 21-35, <https://doi.org/10.1139/t84-003>, 1984.

765 Delle Piane, C., Almqvist, B.S., MacRae, C.M., Torpy, A., Mory, A.J. and Dewhurst, D.N.: Texture and diagenesis
766 of Ordovician shale from the Canning Basin, Western Australia: Implications for elastic anisotropy and
767 geomechanical properties. *Marine and Petroleum Geology*, 59, 56-71, <doi.org/10.1016/j.marpetgeo.2014.07.017>,
768 2015.

769 Den Hartog, S. A. and Spiers, C. J.: A microphysical model for fault gouge friction applied to subduction
770 megathrusts, *Journal of Geophysical Research: Solid Earth*, 119(2), 1510-1529.
771 <https://doi.org/10.1002/2013JB010580>, 2014.

772 Desbois, G., Urai, J.L. and Kukla, P.A.: Morphology of the pore space in claystones—evidence from BIB/FIB ion
773 beam sectioning and cryo-SEM observations. *eEarth Discussions*, 4(1), 1-19, 2009.

774 Desbois, G., Urai, J.L., Hemes, S., Brassinnes, S., De Craen, M. and Sillen, X.: Nanometer-scale pore fluid
775 distribution and drying damage in preserved clay cores from Belgian clay formations inferred by BIB-cryo-
776 SEM. *Engineering Geology*, 179, 117-131, <https://doi.org/10.1016/j.enggeo.2014.07.004>, 2014.

777 Desbois, G., Höhne, N., Urai, J. L., Bésuelle, P., and Viggiani, G.: Deformation in cemented mudrock (Callovo–
778 Oxfordian Clay) by microcracking, granular flow and phyllosilicate plasticity: insights from triaxial deformation,
779 broad ion beam polishing and scanning electron microscopy, *Solid Earth*, 8, 291–305, [https://doi.org/10.5194/se-](https://doi.org/10.5194/se-8-291-2017)
780 [8-291-2017](https://doi.org/10.5194/se-8-291-2017), 2017.

781 Desbois, G., Urai, J. L., Kukla, P. A., Konstanty, J., & Baerle, C.: High-resolution 3D fabric and porosity model
782 in a tight gas sandstone reservoir: A new approach to investigate microstructures from mm-to nm-scale combining
783 argon beam cross-sectioning and SEM imaging. *Journal of Petroleum Science and Engineering*, 78(2), 243-257,
784 <https://doi.org/10.1016/j.petrol.2011.06.004>, 2011.

785 Djeran-Maigre, I., Tessier, D., Grunberger, D., Velde, B. and Vasseur, G.: Evolution of microstructures and of
786 macroscopic properties of some clays during experimental compaction. *Marine and Petroleum Geology*, 15(2),
787 109-128, [doi.org/10.1016/S0264-8172\(97\)00062-7](https://doi.org/10.1016/S0264-8172(97)00062-7), 1998.

788 Dugan, B., McNeill, L. and Petronotis, K.: Expedition 362 preliminary report: Sumatra subduction zone,
789 International Ocean Discovery Program, 2017.

790 Dutilleul, J., Bourlange, S., Conin, M. and Géraud, Y.: Quantification of bound water content, interstitial porosity
791 and fracture porosity in the sediments entering the North Sumatra subduction zone from Cation Exchange Capacity
792 and IODP Expedition 362 resistivity data, *Marine and Petroleum Geology*, 111, 156-165.,
793 <https://doi.org/10.1016/j.marpetgeo.2019.08.007>, 2020.

794 Ehrenberg, S. N.: Assessing the relative importance of compaction processes and cementation to reduction of
795 porosity in sandstones: discussion. *American Association of Petroleum Geologists Bulletin*, 73, 1274-1276,
796 <https://doi.org/10.1306/44B4AA1E-170A-11D7-8645000102C1865D>, 1989.

797 Elliott, J.A., Windle, A.H., Hobdell, J.R., Eeckhaut, G., Oldman, R.J., Ludwig, W., Boller, E., Cloetens, P. and
798 Baruchel, J.: In-situ deformation of an open-cell flexible polyurethane foam characterised by 3D computed
799 microtomography, *Journal of materials science*, 37(8), 1547-1555, doi:10.1023/A:1014920902712, 2002.

800 Emmanuel, S. and Day-Stirrat, R.J.: 2012. A framework for quantifying size dependent deformation of nano-scale
801 pores in mudrocks *Journal of applied geophysics*, 86, 29-35, <https://doi.org/10.1016/j.jappgeo.2012.07.011>, 2012.

802 Fawad, M., Mondol, N.H., Jahren, J. and Bjørlykke, K.: Microfabric and rock properties of experimentally
803 compressed silt-clay mixtures, *Marine and Petroleum Geology*, 27(8), 1698-1712,
804 <https://doi.org/10.1016/j.marpetgeo.2009.10.002>, 2010.

805 Fossen, H.: *Structural geology*. Cambridge university press. 2016.

806 Ghosal, D., Singh, S.C. and Martin, J.: Shallow subsurface morphotectonics of the NW Sumatra subduction system
807 using an integrated seismic imaging technique, *Geophysical Journal International*, 198(3), 1818-1831,
808 <https://doi.org/10.1093/gji/ggu182>, 2014.

809 Griffiths, F.J. and Joshi, R.C.: Change in pore size distribution due to consolidation of clays. *Geotechnique*, 39(1),
810 159-167, doi.org/10.1680/geot.1989.39.1.159, 1989.

811 Griffiths, F.J. and Joshi, R.C.: Clay fabric response to consolidation. *Applied clay science*, 5(1), 37-66,
812 [doi.org/10.1016/0169-1317\(90\)90005-A](https://doi.org/10.1016/0169-1317(90)90005-A), 1990.

813 Griffiths, F.J. and Joshi, R.C.: Change in pore size distribution owing to secondary consolidation of
814 clays. *Canadian Geotechnical Journal*, 28(1), 20-24, <https://doi.org/10.1139/t91-003>, 1991.

815 Hemes, S., Desbois, G., Klaver, J. and Urai, J.L.: Microstructural characterisation of the Ypresian clays (Kallo-1)
816 at nanometre resolution, using broad-ion beam milling and scanning electron microscopy. *Netherlands Journal of*
817 *Geosciences*, 95(3), 293-313, DOI: <https://doi.org/10.1017/njg.2016.16>, 2016.

818 Hemes, S., Desbois, G., Urai, J.L., De Craen, M. and Honty, M.: Variations in the morphology of porosity in the
819 Boom Clay Formation: insights from 2D high resolution BIB-SEM imaging and Mercury injection
820 Porosimetry. *Netherlands Journal of geosciences*, 92(4), 275-300, DOI: doi.org/10.1017/S0016774600000214,
821 2013.

822 Hemes, S., Desbois, G., Urai, J.L., Schröppel, B. and Schwarz, J.O.: Multi-scale characterization of porosity in
823 Boom Clay (HADES-level, Mol, Belgium) using a combination of X-ray μ -CT, 2D BIB-SEM and FIB-SEM
824 tomography. *Microporous and mesoporous materials*, 208, 1-20, [https://](https://doi.org/10.1016/j.micromeso.2015.01.022)
825 doi.org/10.1016/j.micromeso.2015.01.022, 2015.

826 Hesse, R.: Turbiditic and non-turbiditic mudstone of Cretaceous flysch sections of the East Alps and other
827 basins. *Sedimentology*, 22(3), 387-416, <https://doi.org/10.1111/j.1365-3091.1975.tb01638.x>, 1975.

828 **Hippchen, S. and Hyndman, R.D.: Thermal and structural models of the Sumatra subduction zone: Implications**
829 **for the megathrust seismogenic zone. *Journal of Geophysical Research: Solid Earth*, 113(B12), [https://doi.org/10.](https://doi.org/10.1029/2008JB006391)**
830 **<https://doi.org/10.1029/2015TC003901>, 2008.**

831 Ho, N.C., Peacor, D.R. and Van der Pluijm, B.A.: Preferred orientation of phyllosilicates in Gulf Coast mudstones
832 and relation to the smectite-illite transition. *Clays and Clay Minerals*, 47(4), 495-504, DOI: 10.1346/CCMN.
833 1999.0470412, 1999.

834 Houben, M.E., Desbois, G. and Urai, J.L.: A comparative study of representative 2D microstructures in Shaly and
835 Sandy facies of Opalinus Clay (Mont Terri, Switzerland) inferred from BIB-SEM and MIP methods, *Marine and*
836 *Petroleum Geology*, 49, 143-161, <https://doi.org/10.1016/j.marpetgeo.2013.10.009>, 2014.

837 Hüpers, A., Ikari, M.J., Dugan, B., Underwood, M.B. and Kopf, A.J.: Origin of a zone of anomalously high
838 porosity in the subduction inputs to Nankai Trough. *Marine Geology*, 361, 147-162,
839 <https://doi.org/10.1016/j.margeo.2015.01.004>, 2015.

840 Hüpers, A., Torres, M.E., Owari, S., McNeill, L.C., Dugan, B., Henstock, T.J., Milliken, K.L., Petronotis, K.E.,
841 Backman, J., Bourlange, S. and Chemale, F.: Release of mineral-bound water prior to subduction tied to shallow
842 seismogenic slip off Sumatra. *Science*, 356(6340), 841-844. 2017.

843 Jiang, M., Klaver, J., Schmatz, J. and Urai, J.L.: Nanoscale porosity analysis in geological materials. *Acta*
844 *Stereologica*, 2015.

845 Kameda, A., Dvorkin, J., Keehm, Y., Nur, A. and Bosl, W.: Permeability-porosity transforms from small sandstone
846 fragments. *Geophysics*, 71(1), N11-N19, <https://doi.org/10.1190/1.2159054>, 2006.

847 Karaborni, S., Smit, B., Heidug, W., Urai, J. and Van Oort, E.: The swelling of clays: molecular simulations of
848 the hydration of montmorillonite. *Science*, 271(5252), 1102-1104, DOI: 10.1126/science.271.5252.1102, 1996.

849 Klaver, J., Desbois, G., Littke, R. and Urai, J.L.: BIB-SEM characterization of pore space morphology and
850 distribution in postmature to overmature samples from the Haynesville and Bossier Shales. *Marine and petroleum*
851 *Geology*, 59, 451-466, <https://doi.org/10.1016/j.marpetgeo.2014.09.020>, 2015.

852 Klaver, J., Desbois, G., Littke, R. and Urai, J.L.: BIB-SEM pore characterization of mature and post mature
853 Posidonia Shale samples from the Hils area, Germany. *International Journal of Coal Geology*, 158, 78-89,
854 <https://doi.org/10.1016/j.coal.2016.03.003>, 2016.

855 Klaver, J., Desbois, G., Urai, J.L. and Littke, R.: BIB-SEM study of the pore space morphology in early mature
856 Posidonia Shale from the Hils area, Germany. *International Journal of Coal Geology*, 103, 12-25.
857 <https://doi.org/10.1016/j.coal.2012.06.012>, 2012.

858 Kuila, U. and Prasad, M.: Specific surface area and pore-size distribution in clays and shales. *Geophysical*
859 *Prospecting*, 61(2-Rock Physics for Reservoir Exploration, Characterisation and Monitoring), pp.341-362,
860 <https://doi.org/10.1111/1365-2478.12028>, 2013.

861 Lander, R. H. and Walderhaug, O. W.: Predicting porosity through simulating sandstone compaction and quartz
862 cementation. *American Association of Petroleum Geologists Bulletin* 83: 433-449,
863 <https://doi.org/10.1306/00AA9BC4-1730-11D7-8645000102C1865D>, 1999.

864 Lander, R. H., Larese, R. H. Larese and Bonnell, L. M.: Toward more accurate quartz cement models: The
865 importance of euhedral versus noneuhedral growth rates. *American Association Petroleum Geologists Bulletin* 92:
866 1537-1563. <https://doi.org/10.1306/07160808037>, 2008.

867 Laurich, B., Urai, J.L., Desbois, G., Vollmer, C. and Nussbaum, C.: Microstructural evolution of an incipient fault
868 zone in Opalinus Clay: Insights from an optical and electron microscopic study of ion-beam polished samples from
869 the Main Fault in the Mt-Terri Underground Research Laboratory. *Journal of Structural Geology*, 67, 107-128.
870 <https://doi.org/10.1016/j.jsg.2014.07.014>, 2014.

871 Lay, T., Kanamori, H., Ammon, C. J., Nettles, M., Ward, S.N., Aster, R.C., Beck, S.L., Bilek, S.L., Brudzinski,
872 M.R., Butler, R. and DeShon, H.R.: The great Sumatra-Andaman earthquake of 26 Ddecember
873 2004. *Sscience*, 308(5725), pp.1127-1133, DOI: 10.1126/science.1112250, 2005.

874 Lazar, O.R., Bohacs, K.M., Macquaker, J.H., Schieber, J. and Demko, T.M.: Capturing key attributes of fine-
875 grained sedimentary rocks in outcrops, cores, and thin sections: nomenclature and description guidelines. *Journal*
876 *of Sedimentary Research*, 85(3), pp.230-246, <https://doi.org/10.2110/jsr.2015.11>, 2015.

877 Lundegard, P. D.: Sandstone porosity loss--a 'big picture' view of the importance of compaction. *Journal of*
878 *Sedimentary Petrology* 62: 250-260, <https://doi.org/10.1306/D42678D4-2B26-11D7-8648000102C1865D>, 1992.

879 March, A.: Mathematical theory of the Korngestah control for affine deformation. *Journal of Crystallography-*
880 *Crystalline Materials*, 81 (1-6), 285-297, doi.org/10.1524/zkri.1932.81.1.285, 1932.

881 McNeill, L.C., Dugan, B. and Petronotis, K.E., Backman, J., Bourlange, S., Chemale, F., Chen, W., Colson, T.A.,
882 Frederik, M.C.G., Guèrin, G., Hamahashi, M., Henstock, T., House, B.M., Hüpers, A., Jeppson, T.N., Kachovich,
883 S., Kenigsberg, A.R., Kuranaga, M., Kutterolf, S., Milliken, K.L., Mitchison, F.L., Mukoyoshi, H., Nair, N.,
884 Owari, S., Pickering, K.T., Pouderoux, H.F.A., Yehua, S., Song, I., Torres, M.E., Vannucchi, P., Vrolijk, P.J.,
885 Yang, T., and Zhao, X.: Sumatra Subduction Zone. *Proceedings of the International Ocean Discovery*
886 *Program*, 362, <https://doi.org/10.14379/iodp.proc.362.102.2017>, 2017a.

887 McNeill, L.C., Dugan, B. and Petronotis, K.E., Backman, J., Bourlange, S., Chemale, F., Chen, W., Colson, T.A.,
888 Frederik, M.C.G., Guèrin, G., Hamahashi, M., Henstock, T., House, B.M., Hüpers, A., Jeppson, T.N., Kachovich,
889 S., Kenigsberg, A.R., Kuranaga, M., Kutterolf, S., Milliken, K.L., Mitchison, F.L., Mukoyoshi, H., Nair, N.,
890 Owari, S., Pickering, K.T., Pouderoux, H.F.A., Yehua, S., Song, I., Torres, M.E., Vannucchi, P., Vrolijk, P.J.,
891 Yang, T., and Zhao, X.: Sumatra Subduction Zone. *Proceedings of the International Ocean Discovery*
892 *Program*, 362, (Supplementary material), <https://doi.org/10.14379/iodp.proc.362supp.2017>, 2017b.

893 Meade, R.H.: Removal of water and rearrangement of particles during the compaction of clayey sediments. US
894 Government Printing Office, 1964.

895 Mesri, G. and Olson, R.E.: Mechanisms controlling the permeability of clays. *Clays and Clay minerals*, 19(3),
896 151-158, 1971.

897 Milliken, K. L.: A compositional classification for grain assemblages in fine-grained sediments and sedimentary
898 rocks. *Journal of Sedimentary Research* 84: 1185-1199, <https://doi.org/10.2110/jsr.2014.92>, 2008.

899 Milliken, K. L.: A compositional classification for grain assemblages in fine-grained sediments and sedimentary
900 rocks. *Journal of Sedimentary Research* 84: 1185-1199, <https://doi.org/10.2110/jsr.2014.92>, 2014.

901 Milliken K. L.: Compactional and mass-balance constraints inferred from the volume of quartz cementation in
902 mudrocks. *Mudstone Diagenesis: New Research Perspectives for Shale Hydrocarbon Reservoirs, Seals, and*
903 *Source Rocks*. AAPG. 120: 33-48, DOI: 10.1306/13672209M121252, 2019.

904 Milliken, K. L. and Curtis, M. E.: Imaging pores in sedimentary rocks: Foundation of porosity prediction. *Marine*
905 *and Petroleum Geology* 73,: 590-608, <https://doi.org/10.1016/j.marpetgeo.2016.03.020>, 2016.

906 Milliken, K. L. and Day-Stirrat R. J.: Cementation in mudrocks: Brief review with examples from cratonic basin
907 mudrocks. *Memoir. J.-Y. Chatellier*. Tulsa, Oklahoma, USA, AAPG, <https://doi.org/10.1306/13401729H55252>,
908 2013.

909 Milliken, K. L. and Olson, T.: Silica diagenesis, porosity evolution, and mechanical behavior in siliceous
910 mudstones, Mowry Shale Cretaceous, Rocky Mountains, U.S.A. *Journal of Sedimentary Research* 87: 366-387,
911 [.https://doi.org/10.2110/jsr.2017.24](https://doi.org/10.2110/jsr.2017.24), 2017.

912 Milliken, K. L., Rudnicki, M., Awwiller, D. N. and Zhang, T.: Organic matter-hosted pore system, Marcellus
913 Formation Devonian, Pennsylvania, USA. *AAPG Bulletin* 97: 177-200, <https://doi.org/10.1306/07231212048>,
914 2013.

915 Milliken, K.L. and Reed, R.M.: Multiple causes of diagenetic fabric anisotropy in weakly consolidated mud,
916 Nankai accretionary prism, IODP Expedition 316. *Journal of Structural Geology*, 32(12), 1887-1898,
917 doi.org/10.1016/j.jsg.2010.03.008, 2010.

918 Milliken, K. L., Esch, W. L., Reed, R. M. and Zhang, T.: Grain assemblages and strong diagenetic overprinting
919 in siliceous mudrocks, Barnett Shale Mississippian, Fort Worth Basin, Texas, U.S.A. *AAPG Bulletin* 96: 1553-
920 1578, <https://doi.org/10.1306/12011111129>, 2012.

921 Mitchell, J.K.: The fabric of natural clays and its relation to engineering properties. In *Highway Research Board*
922 *Proceedings*, 35, 1956.

923 Moeremans, R.E. and Singh, S.C.: Fore-arc basin deformation in the Andaman-Nicobar segment of the Sumatra-
924 Andaman subduction zone: Insight from high-resolution seismic reflection data, *Tectonics*, 34(8), 1736-1750,
925 doi.org/10.1002/2015TC003901, 2015.

926 Mondol, N.H., Bjørlykke, K., Jahren, J. and Høeg, K.: Experimental mechanical compaction of clay mineral
927 aggregates—Changes in physical properties of mudstones during burial. *Marine and petroleum geology*, 24(5),
928 289-311, <https://doi.org/10.1016/j.marpetgeo.2007.03.006>, 2007.

929 Morgenstern, N.R. and Tchalenko, J.S.: Microstructural observations on shear zones from slips in natural clays,
930 1967.

931 Nakano, R.: On weathering and change of properties of tertiary mudstone related to landslide. *Soils and*
932 *Foundations*, 7(1), 1-14, <https://doi.org/10.3208/sandf1960.7.1>, 1967.

933 Neagu, R.C., Cartwright, J. and Davies, R.: Measurement of diagenetic compaction strain from quantitative
934 analysis of fault plane dip. *Journal of Structural Geology*, 32(5), 641-655,
935 <https://doi.org/10.1016/j.jsg.2010.03.010>, 2010.

936 Nole, M., Daigle, H., Milliken, K.L. and Prodanović, M.: A method for estimating microporosity of fine-grained
937 sediments and sedimentary rocks via scanning electron microscope image analysis. *Sedimentology*, 63(6), 1507-
938 1521, <https://doi.org/10.1111/sed.12271>, 2016.

939 Nollet, S., Hilgers, C. and Urai, J.: Sealing of fluid pathways in overpressure cells: a case study from the
940 Buntsandstein in the Lower Saxony Basin (NW Germany). *International Journal of Earth Sciences*, 94(5), 1039-
941 1055, <https://doi.org/10.1007/s00531-005-0492-1>, 2005.

942 Oelker, A.: Deformation properties of Boom Clay: Implementation of a multi-scale concept. Dissertation,
943 Rheinisch-Westfälische Technische Hochschule Aachen, DOI: 10.18154/RWTH-2019-09913, 2019.

944 Oertel, G. and Curtis, C.D.: Clay-ironstone concretion preserving fabrics due to progressive
945 compaction. *Geological Society of America Bulletin*, 83(9), 2597-2606, [https://doi.org/10.1130/0016-7606\(1972\)83\[2597:CCPFD\]2.0.CO;2](https://doi.org/10.1130/0016-7606(1972)83[2597:CCPFD]2.0.CO;2), 1972.

947 Paxton, S. T., J. O. Szabo, J. M. Adjukiewicz and R. E. Klimentidis.: Construction of an intergranular volume
948 compaction curve for evaluating and predicting compaction and porosity loss in rigid-grain sandstone reservoirs.
949 *American Association of Petroleum Geologists Bulletin* 86: 2047-2067, <https://doi.org/10.1306/61EEDDFA-173E-11D7-8645000102C1865D>, 2002.

951 Pickering, K.T., Carter, A., Andò, S., Garzanti, E., Limonta, M., Vezzoli, G. and Milliken, K.L.: 2020. Deciphering
952 relationships between the Nicobar and Bengal submarine fans, Indian Ocean. *Earth and Planetary Science*
953 *Letters*, 544, 116329, <https://doi.org/10.1016/j.epsl.2020.116329>, 2020.

954 Pommer, M. E. and Milliken, K. L.: Pore types and pore-size distributions across thermal maturity, Eagle Ford
955 Formation, South Texas. *AAPG Bulletin* 99: 1713-1744, <https://doi.org/10.1306/03051514151>, 2015.

956 Prawirodirdjo, L., Boel, Y., McCaffrey, R., Genrich, J., Calais, E., Stevens, C., Puntodewo, S.S.O., Subarya, C.,
957 Rais, J., Zwick, P. and Fauzi, R.M.: Geodetic observations of interseismic strain segmentation at the Sumatra
958 subduction zone. *Geophysical research letters*, 24(21), 2601-2604, <https://doi.org/10.1029/97GL52691>, 1997.

959 Rieke, H.H. and Chilingarian, G.V.: *Compaction of argillaceous sediments*. Elsevier, 1974.

960 Rosenberger, K., Underwood, M.B., Vrolijk, P. and Haines, S.: Data report: clay mineral assemblages in
961 hemipelagic sediments entering the Sumatra subduction zone, IODP Sites U1480 and U1481, Expedition
962 362. *Expedition*, 362, 1. 2020.

963 Samsudin, M.S.F., Ariff, Z.M. and Ariffin, A.: Deformation behavior of open-cell dry natural rubber foam: Effect
964 of different concentration of blowing agent and compression strain rate. In *AIP Conference Proceedings*, 1835,
965 No. 1, 020007, AIP Publishing LLC, 2017.

966 Schmatz, J., Klaver, J., Jiang, M. and Urai, J.L.: Nanoscale morphology of brine/oil/mineral contacts in connected
967 pores of carbonate reservoirs: Insights on wettability from Cryo-BIB-SEM. *SPE Journal*, 22(05), 1374-1384,
968 <https://doi.org/10.2118/180049-PA>, 2017.

969 Schneider, J., Flemings, P.B., Day-Stirrat, R.J. and Germaine, J.T.: Insights into pore-scale controls on mudstone
970 permeability through re sedimentation experiments. *Geology*, 39(11), 1011-1014,
971 <https://doi.org/10.1130/G32475.1> , 2011.

972 Sintubin, M.: Clay fabrics in relation to the burial history of shales. *Sedimentology*, 41(6), 1161-1169,
973 <https://doi.org/10.1130/G32475.1>, 1994.

974 Terzaghi, K. and Peck, R.B.: *Soil Mechanics. Engineering Practice*. John Wiley and Sons, Inc., New York, 1948.

975 Torres, M. E., Milliken, K. L., A. Hüpers, J. H. Kim, S. G. Lee: Authigenic clays versus carbonate formation as
976 products of marine silicate weathering in the input sequence to the Sumatra Subduction Zone, *Gechemistry,*
977 *Geophysics Geosystems*, 23 (4), <https://doi.org/10.1029/2022GC010338>, 2022.

978 Ukar, E. and Cloos, M.: Cataclastic deformation and metasomatism in the subduction zone of mafic blocks-in-
979 mélange, San Simeon, California, *Lithos*, 346, 105116, <https://doi.org/10.1016/j.lithos.2019.06.018>, 2019.

980 Underwood, M. B., N. Lawler, and K. McNamara.: Data report: standard mineral mixtures, normalization factors,
981 and determination of error for quantitative X-ray diffraction analyses of bulk powders and clay-sized mineral
982 assemblages. *Proceedings of the International Ocean Discovery Program*, 372,
983 doi.org/10.14379/iodp.proc.372B375.201.2020, 2020.

984 Vasseur, G., Djeran-Maigre, I., Grunberger, D., Rousset, G., Tessier, D. and Velde, B.: Evolution of structural and
985 physical parameters of clays during experimental compaction, *Marine and petroleum geology*, 12(8), pp.941-954,
986 [https://doi.org/10.1016/0264-8172\(95\)98857-2](https://doi.org/10.1016/0264-8172(95)98857-2), 1995.

987 Velde, B.: Compaction trends of clay-rich deep sea sediments, *Marine Geology* 133(3-4): 193-201,
988 [https://doi.org/10.1016/0025-3227\(96\)00020-5](https://doi.org/10.1016/0025-3227(96)00020-5), 1996.

989 Vrolijk, P.: On the mechanical role of smectite in subduction zones. *Geology*, 18(8), pp.703-707,
990 [https://doi.org/10.1130/0091-7613\(1990\)018<0703:OTMROS>2.3.CO;2](https://doi.org/10.1130/0091-7613(1990)018<0703:OTMROS>2.3.CO;2), 1990.

991 Wang, X., Jiang, Z., Jiang, S., Chang, J., Zhu, L., Li, X. and Li, J.: Full-scale pore structure and fractal dimension
992 of the Longmaxi shale from the Southern Sichuan Basin: Investigations using FE-SEM, gas adsorption and
993 mercury intrusion porosimetry. *Minerals*, 9(9), p.543, <https://doi.org/10.3390/min9090543>, 2019.

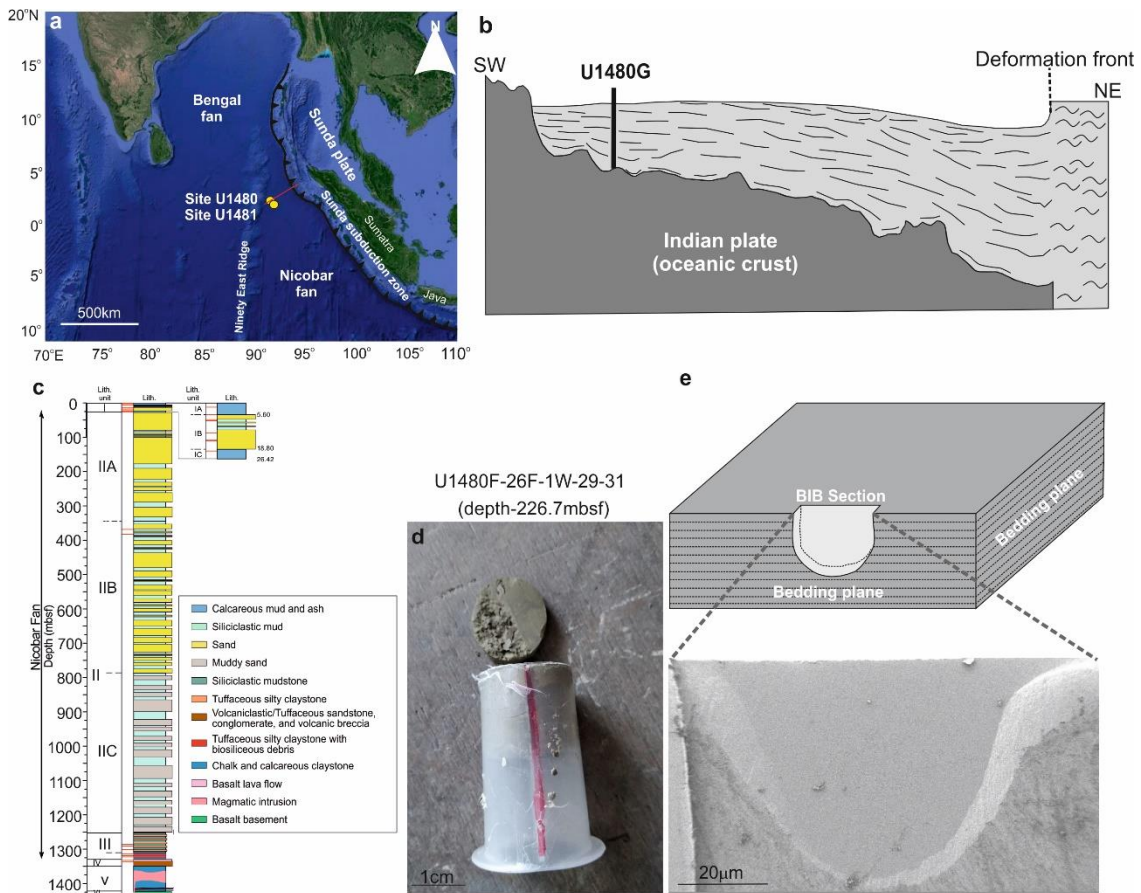
994 Worden, R.H., Charpentier, D., Fisher, Q.J. and Aplin, A.C.: Fabric development and the smectite to illite
995 transition in Upper Cretaceous mudstones from the North Sea: an image analysis approach. *Geological Society,*
996 *London, Special Publications*, 249(1), 103-114, doi.org/10.1144/GSL.SP.2005.249.01.0, 2005.

997 Yagiz, S.: Overview of classification and engineering properties of shales for design considerations.
998 *In Construction and Materials Issues* 2001, 156-165, 2001.

999 Zakaria, Z., Mohamad Ariff, Z. and Abu Bakar, A.: Monitoring deformation mechanism of foam cells in
 1000 polyethylene foams via optical microscopy: Effect of density and microstructure. Journal of Cellular
 1001 Plastics, 54(6), 957-976, <https://doi.org/10.1177/0021955X18795035>, 2018.

1002 Zhou, J., Shrotriya, P. and Soboyejo, W.O.: Mechanisms and mechanics of compressive deformation in open-cell
 1003 Al foams. Mechanics of Materials, 36(8), 781-797, <https://doi.org/10.1016/j.mechmat.2003.05.004>, 2004.

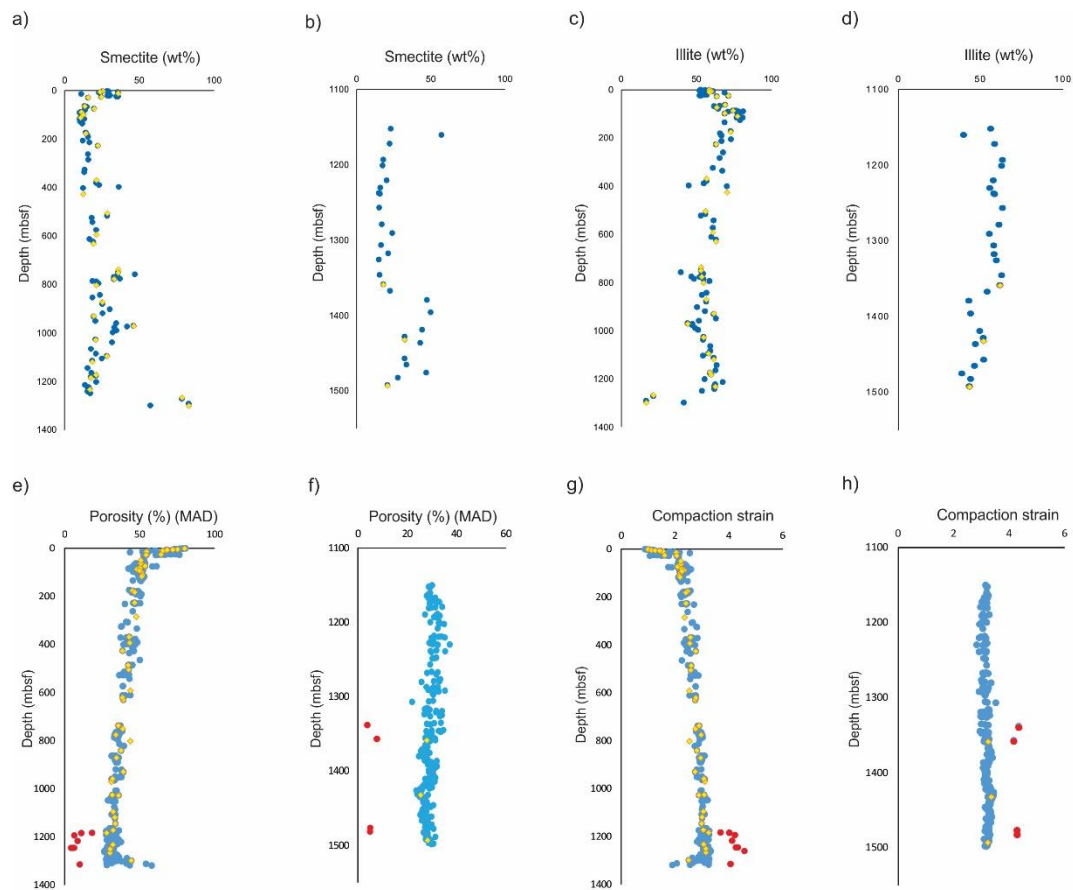
1004



1005

1006 **Fig.1:** (a) Satellite image of Sumatra subduction zone and location of U1480 and U1481 drilling sites (created
 1007 from © Google Maps). (b) Schematic diagram showing location of primary drilling site and deepest drill hole
 1008 (Hole G) at site U1480 in sectional view (adapted from seismic profile from SW to NE after Hüpers et al., 2017).
 1009 Location and extension of the seismic profile is represented by red line in (a). (c) Lithostratigraphic units
 1010 encountered at Site U1480 (adapted after McNeill et al., 2017a). (d) Representative tube sample received from
 1011 IODP repository, Japan. Red-colored line on tube surface represents notch used to denote orientation of samples
 1012 collected from drill core. (e) Representative BIB cross-section polished perpendicular to bedding plane.

1013



1014 **Fig.2:** Depth profiles of smectite content (wt%; clay fraction) for Sites U1480 (a) and U1481 (b) (blue symbol).
 1015 Depth profiles of illite content (wt%; clay fraction) for Sites U1480 (a) and U1481 (b) (blue symbol). Yellow
 1016 symbols indicate samples analyzed by SEM imaging. (e) and (f) Shipboard MAD (Moisture and density) porosity
 1017 profiles for mudstone samples recovered from Sites U1480 and U1481 (blue symbol). (g) and (h) Calculated
 1018 compaction strain profiles for Sites U1480 and U1481 (blue symbols). Red-colored points are cemented
 1019 (concretion) samples. Clay mineralogy data plotted from Rosenberger et al. (2020), and MAD data extracted from
 1020 McNeill et al. (2017**b**).

1021

1022

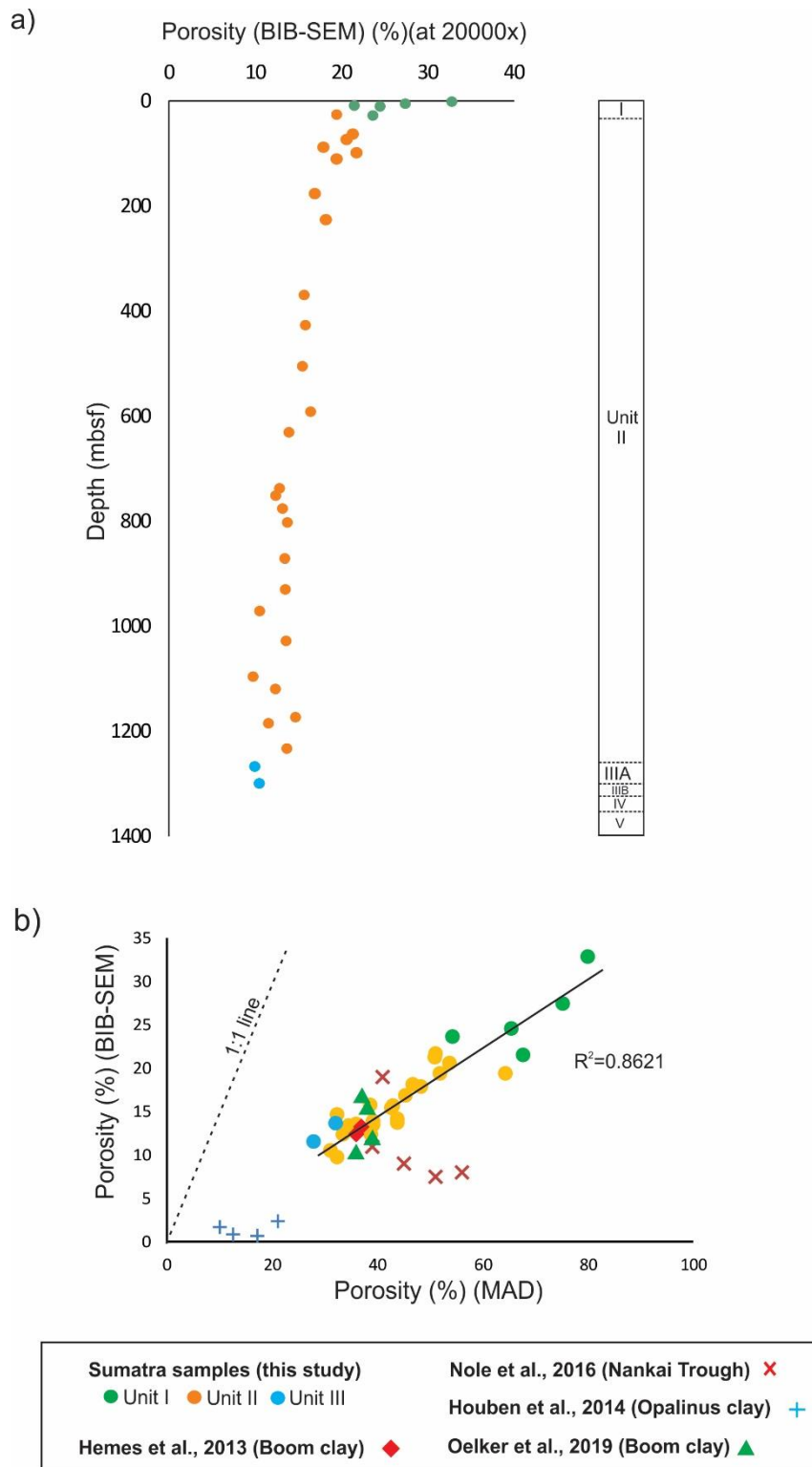
1023

1024

1025

1026

1027

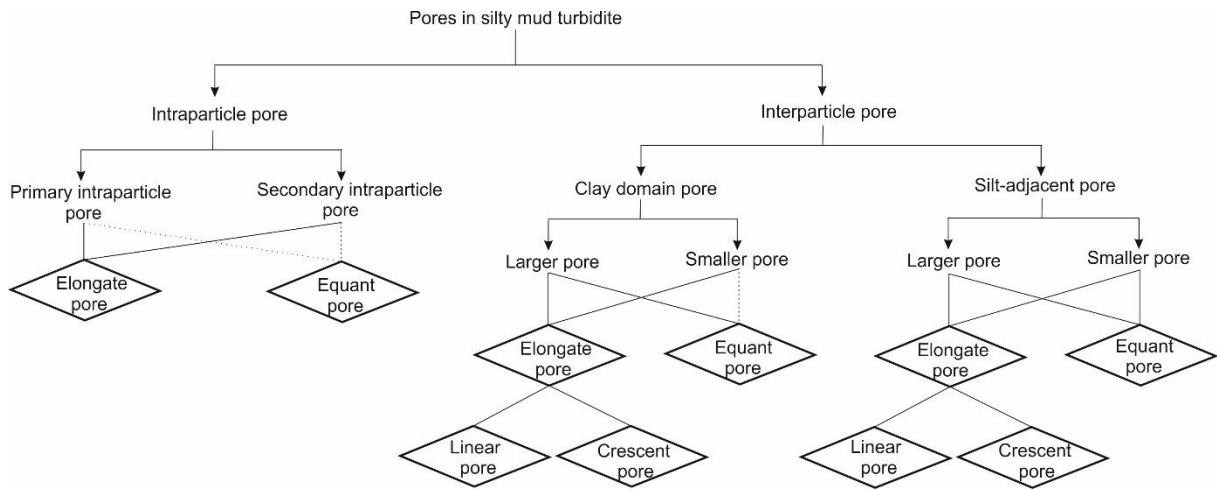


1028

1029 **Fig.3:** Porosity data for Units I (green dots), II (orange dots), and IIIA (blue dots). (a) BIB-SEM porosity - depth
 1030 plot, (b) BIB-SEM porosity vs MAD porosity. Note: linear relationship that intersects origin. Data reported by
 1031 Hemes et al. (2013); Houben et al. (2014); and Oelker et al. (2019) follow similar trend. However, data estimated
 1032 from Nole et al. (2016) deviates from trend.

1033

1034



1035

1036

1037 **Fig.4:** Classification scheme adopted to demonstrate pore reduction mechanics with increasing compactional
1038 strain. Dashed lines indicate rare pore types.

1039

1040

1041

1042

1043

1044

1045

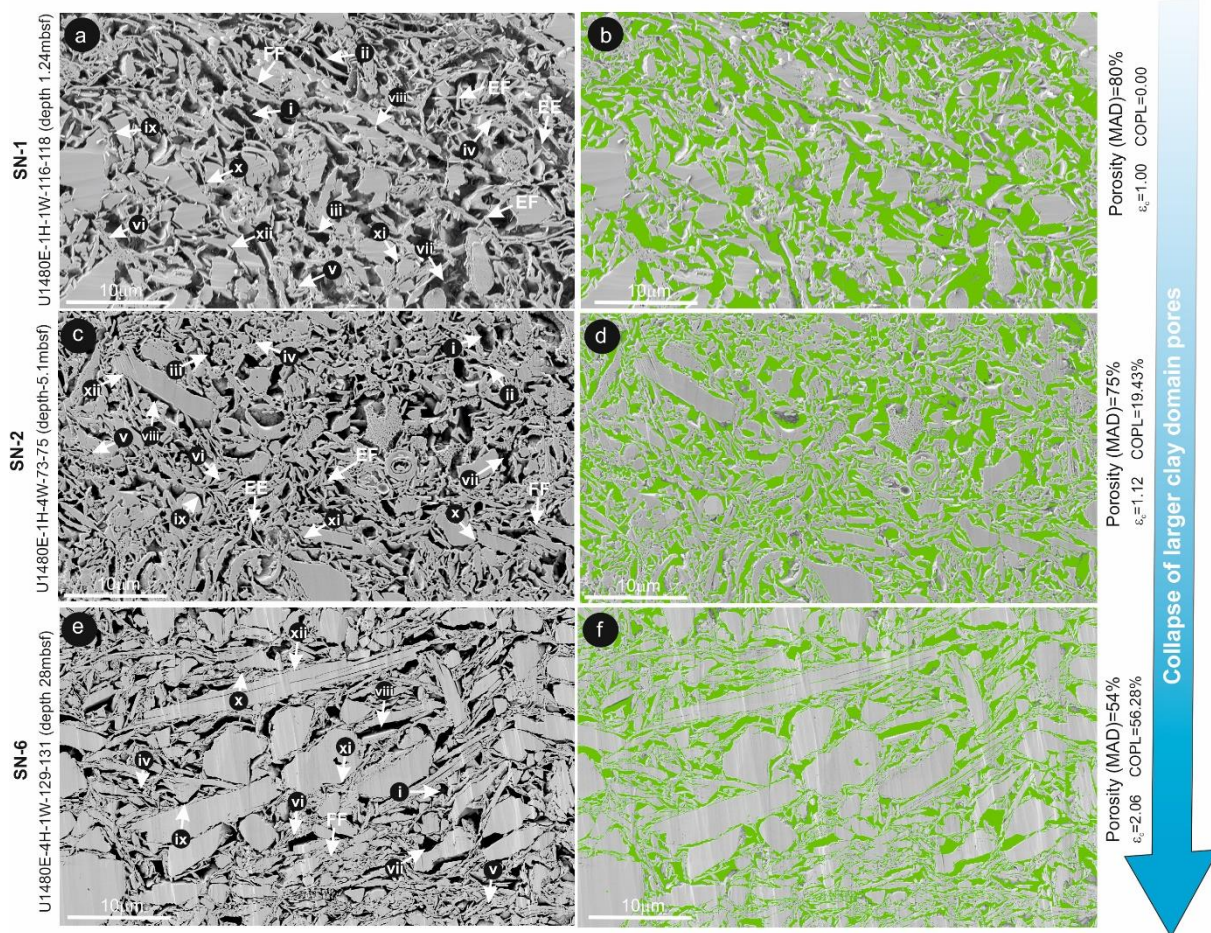
1046

1047

1048

1049

1050



1051

1052 **Fig.5:** Microstructural overview (BIB-SEM) of samples SN-1 (a and b), SN-2 (c and d), and SN-6 (e and f). Green
 1053 color represents segmented pores of the corresponding microstructure of sample. i = Equant large clay domain
 1054 pores, ii = elongated large clay domain pores, iii = Crescent-shaped large clay domain pores, iv = equant small
 1055 clay domain pores, v = Crescent-shaped small clay domain pores, vi = elongated small clay domain pores, vii =
 1056 Equant large silt-adjacent pores, viii = elongated large silt-adjacent pores, ix = Crescent-shaped large silt-adjacent
 1057 pores, x = equant small silt-adjacent pores, xi = Crescent-shaped small silt-adjacent pores, xii = elongated small
 1058 silt-adjacent pores. EE= Edge to edge contact, EF=Edge to face contact, and FF=Face to face contact.

1059

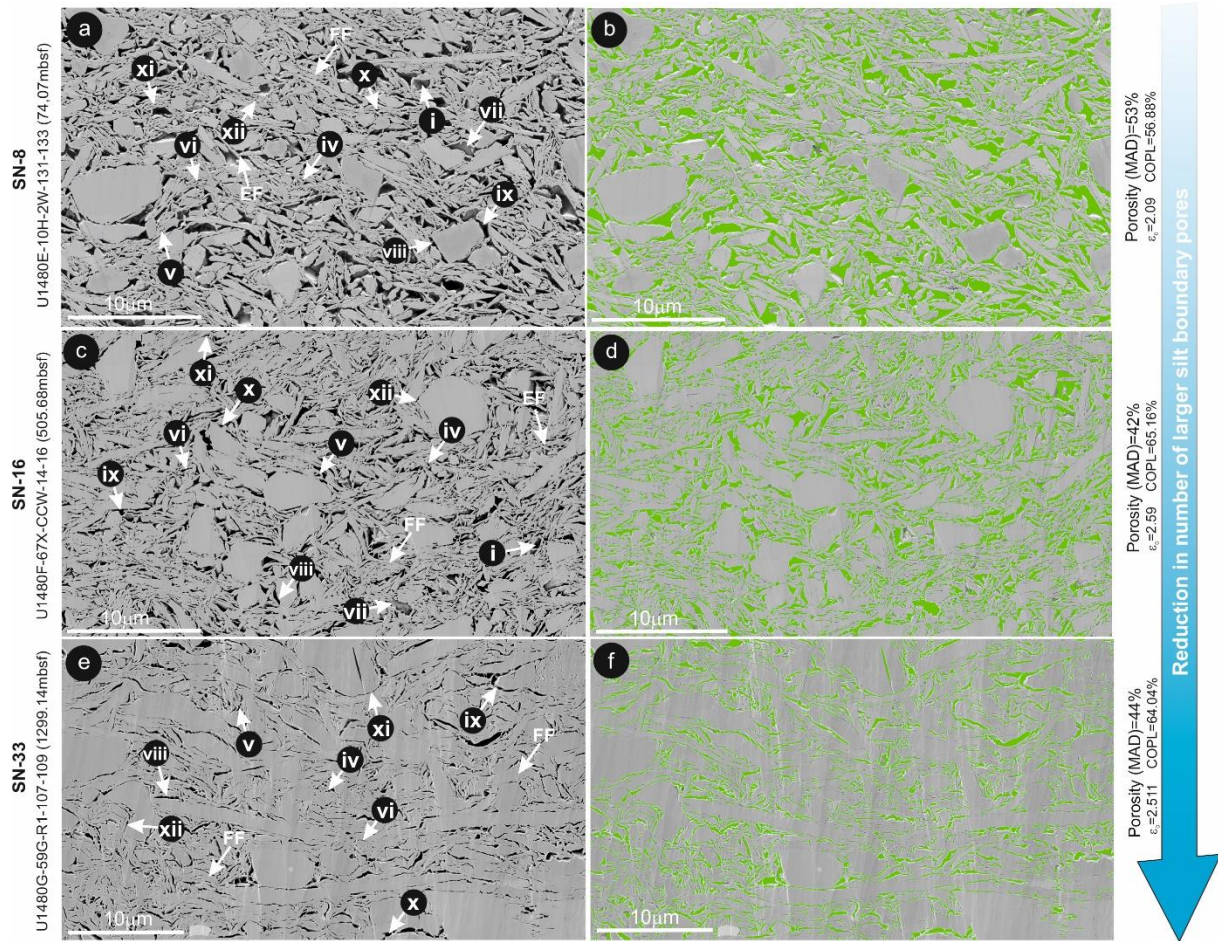
1060

1061

1062

1063

1064



1065

1066 **Fig.6:** Microstructural overview (BIB-SEM) of samples SN-8 (a and b), SN-16 (c and d), and SN-33 (e and f).
 1067 Green color represents segmented pores of the corresponding microstructure of sample. i = Equant large clay
 1068 domain pores, ii = elongated large clay domain pores, iii = Crescent-shaped large clay domain pores, iv = equant
 1069 small clay domain pores, v = Crescent-shaped small clay domain pores, vi = elongated small clay domain pores,
 1070 vii = Equant large silt-adjacent pores, viii = elongated large silt-adjacent pores, ix = Crescent-shaped large silt-
 1071 adjacent pores, x = equant small silt-adjacent pores, xi = Crescent-shaped small silt-adjacent pores, xii = elongated
 1072 small silt-adjacent pores. FF= Face to face contact, EF= Edge to face contact.

1073

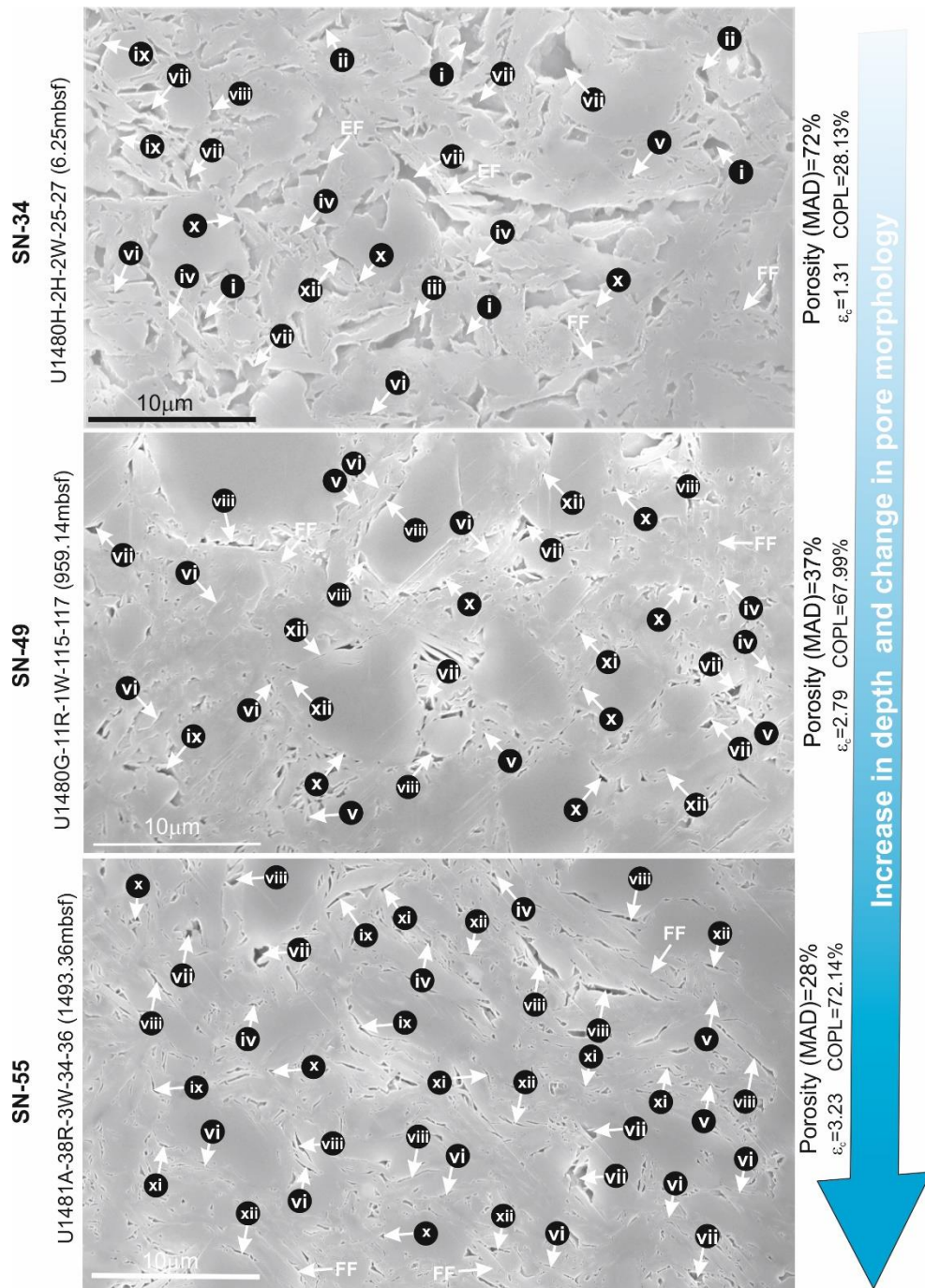
1074

1075

1076

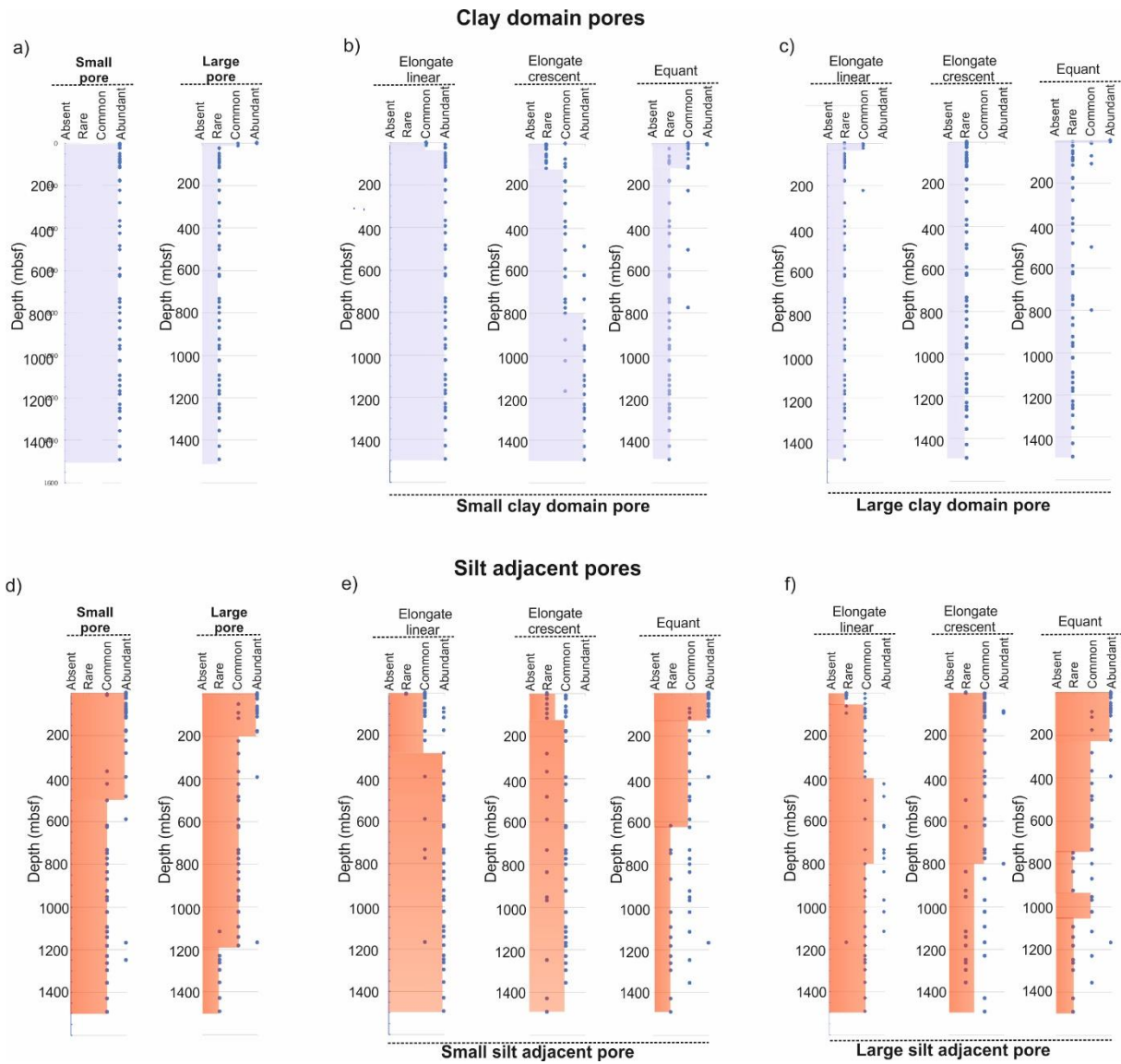
1077

1078

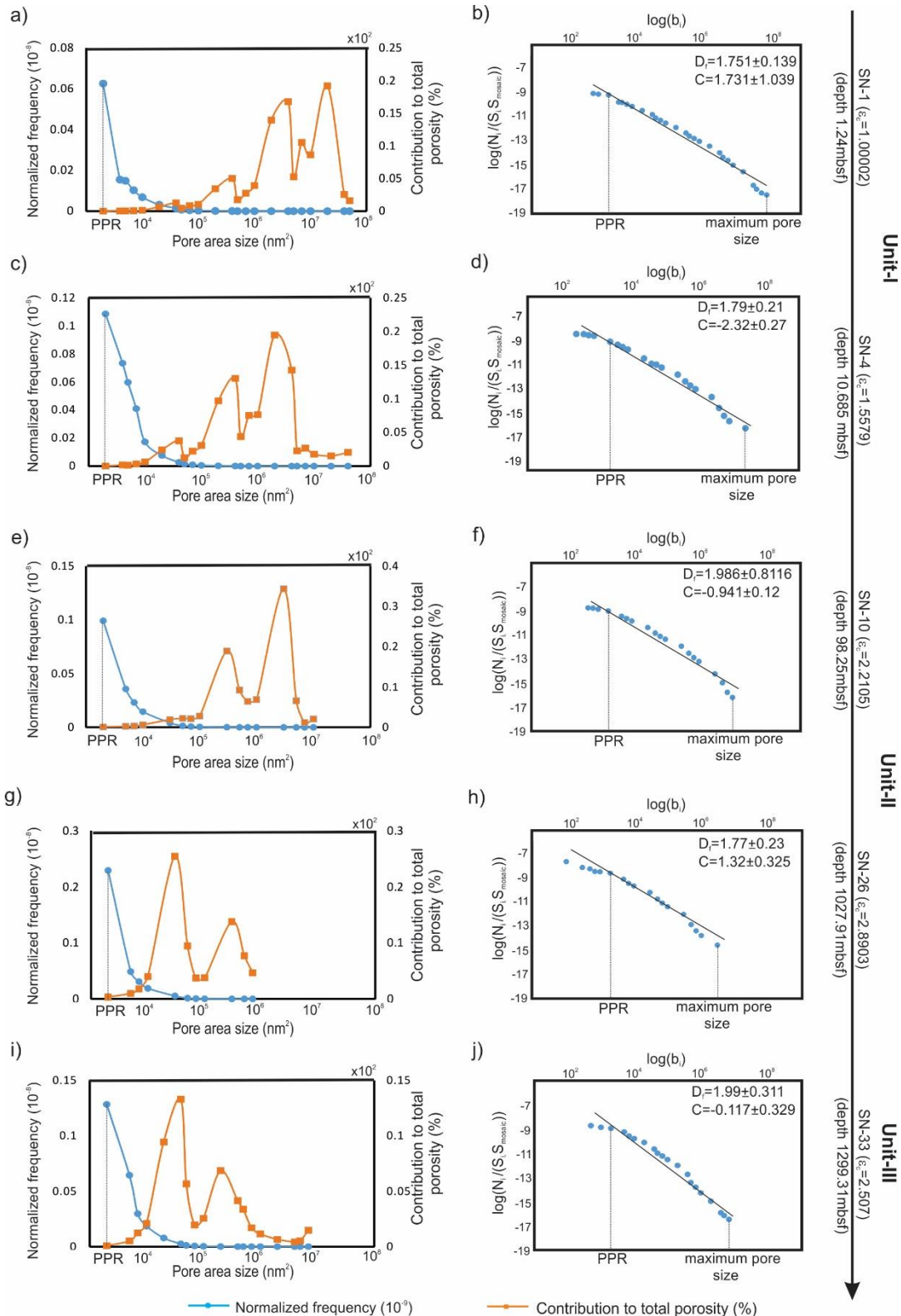


1080

1081 **Fig.7:** Microstructural overview (Field Emission SEM) of samples SN-34, SN-49, and SN-55. i = Equant large
 1082 clay domain pores, ii = elongated large clay domain pores, iii = Crescent-shaped large clay domain pores, iv =
 1083 equant small clay domain pores, v = Crescent-shaped small clay domain pores, vi = elongated small clay domain
 1084 pores, vii = Equant large silt-adjacent pores, viii = elongated large silt-adjacent pores, ix = Crescent-shaped large
 1085 silt-adjacent pores, x = equant small silt-adjacent pores, xi = Crescent-shaped small silt-adjacent pores, xii =
 1086 elongated small silt-adjacent pores. FF= Face to face contact, EF= Edge to face contact.

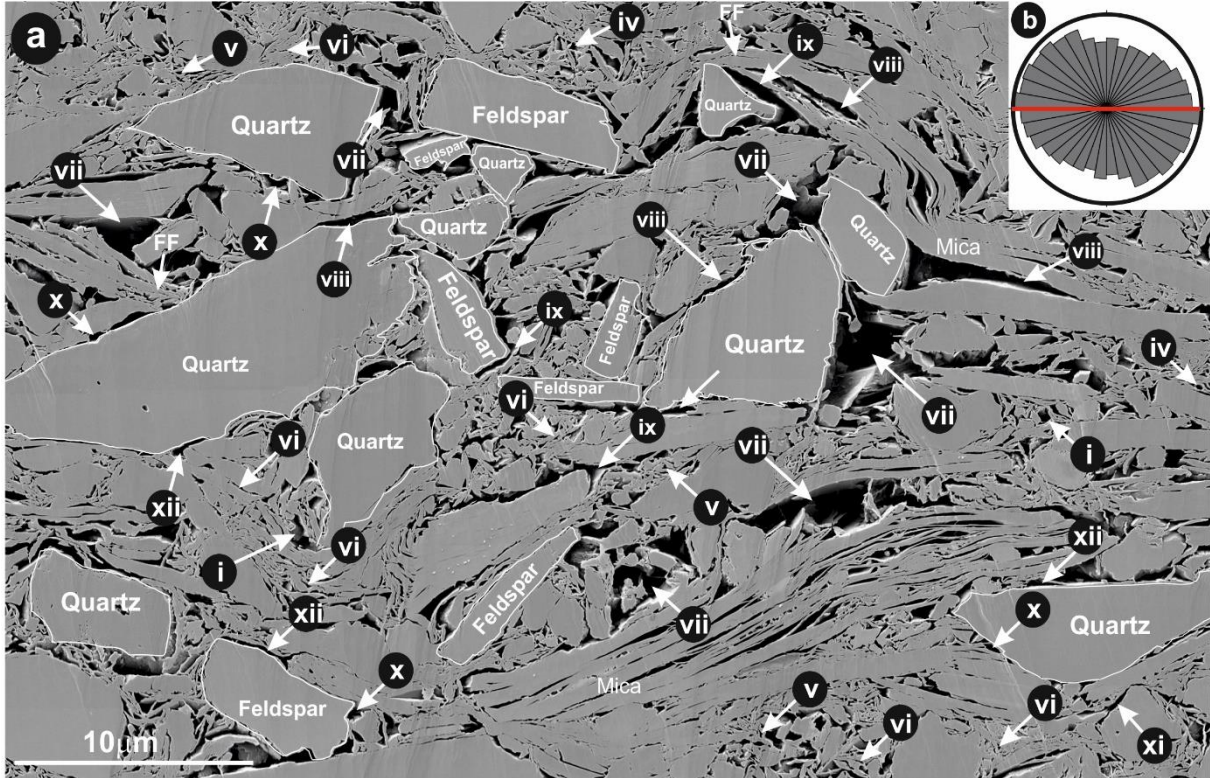


1089 **Fig.8:** Pore type summary for clay domain (a-c) and silt-adjacent (d-f) pore types. (a) abundance of small and large
 1090 clay domain pores; (b) and (c) depth progression of small and large clay domain pore morphologies; (d) abundance
 1091 of small and large silt-adjacent pores; (e) and (f) depth progression of small and large clay domain pore
 1092 morphologies. Abundant = >25% pores, common = 2%-25% pores, rare = 0-2% pores, absent = not observed.



1099 **Fig.9:** Pore size distribution defined by pore area. Left column: normalized frequency (blue) and contribution to
 1100 total porosity (orange). Right column: pore size-frequency log-log distribution. Power-law between PPR and
 1101 maximum pore size interpreted as black line with corresponding regression parameters. Sample number, depth,
 1102 and compaction strain defined along right side of diagram

SN- 29 (U1480G-45R-1W-93-95, depth 1172.88mbsf)



1104

1105

1106 **Fig.10:** Silt-rich sample (SN-29; 1173 mbsf) (a) i = Equant large clay domain pores, ii =elongated large clay
1107 domain pores, iii = Crescent-shaped large clay domain pores, iv = equant small clay domain pores, v = Crescent-
1108 shaped small clay domain pores, vi = elongated small clay domain pores, vii = Equant large silt-adjacent pores,
1109 viii = elongated large silt-adjacent pores, ix = Crescent-shaped large silt-adjacent pores, x =equant small silt-
1110 adjacent pores, xi = Crescent-shaped small silt-adjacent pores, xii = elongated small silt-adjacent pores.(b) Rose
1111 diagram of long axes of pores (bedding = red line). FF= face to face contact of clay particles.

1112

1113

1114

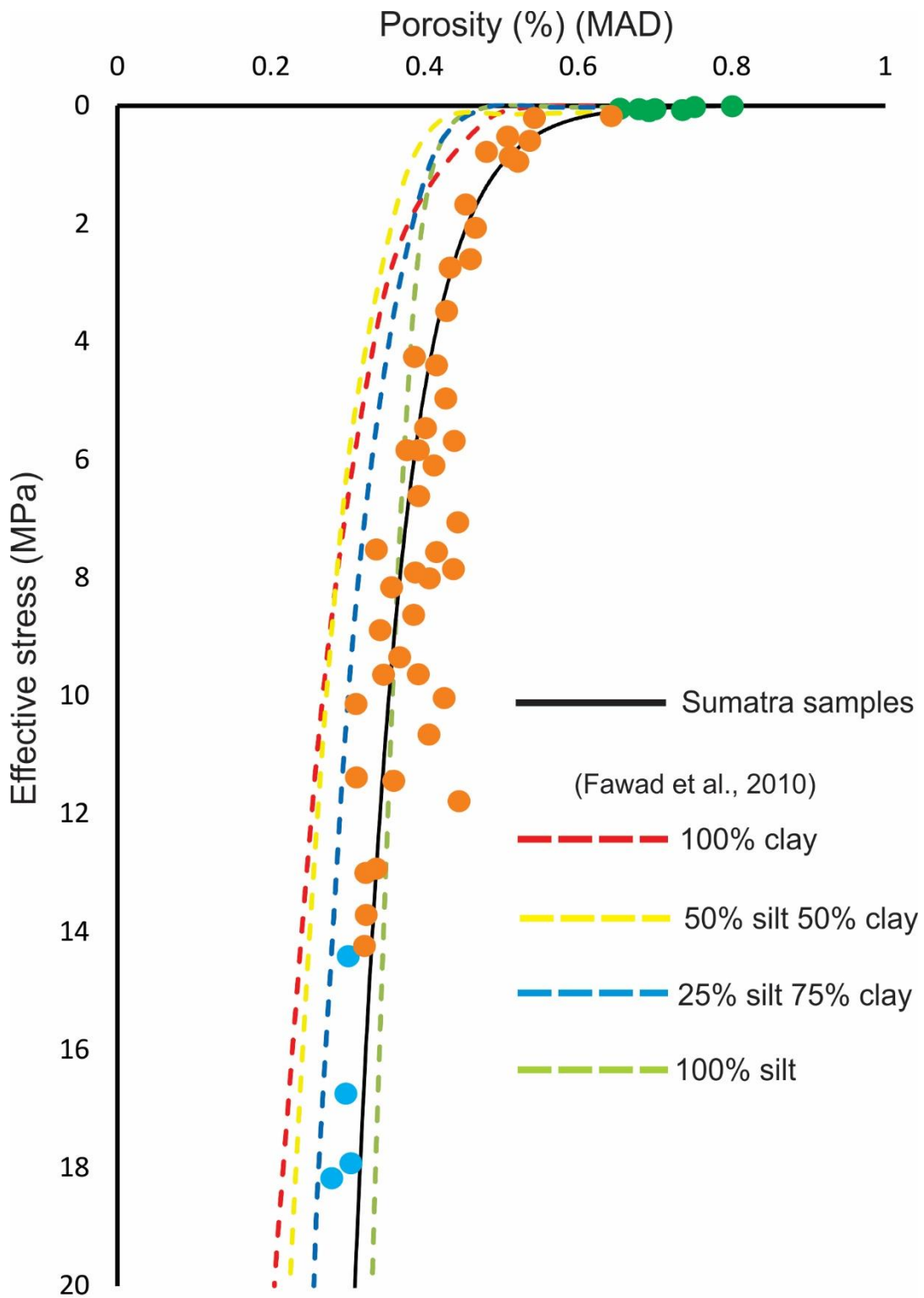
1115

1116

1117

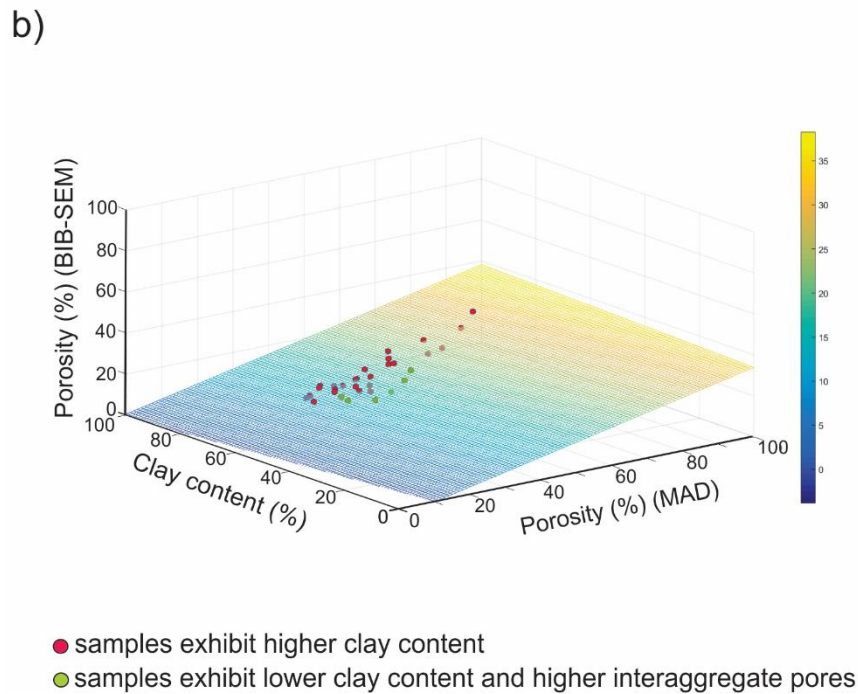
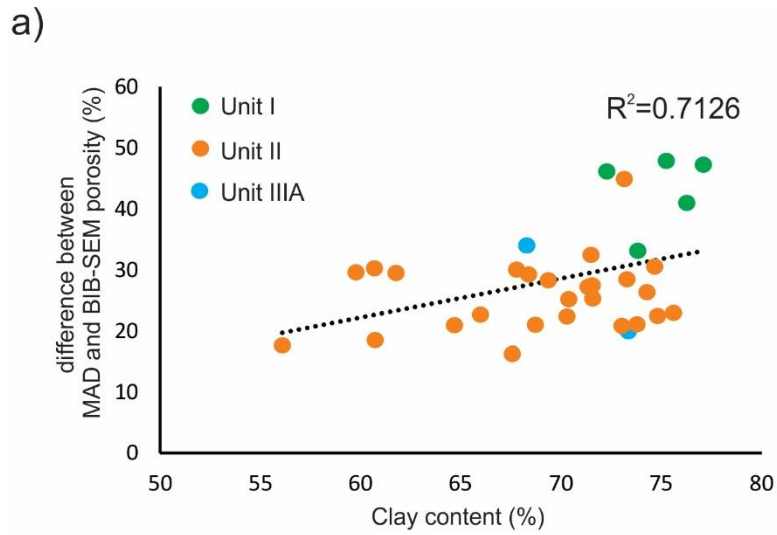
1118

1119



1121

1122 **Fig.11:** Effective stress vs porosity (MAD) for experimental mixtures of clay and silt (dashed lines; Fawad et al.,
 1123 2010) compared with Sumatra data (Unit 1 = green; Unit II = orange; Unit III = blue). Solid black solid line is a
 1124 best-fit data regression for Sumatra samples.



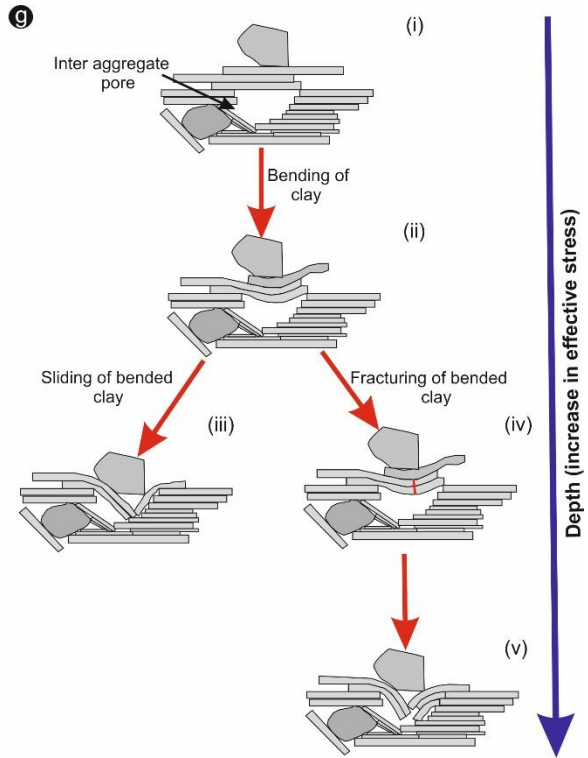
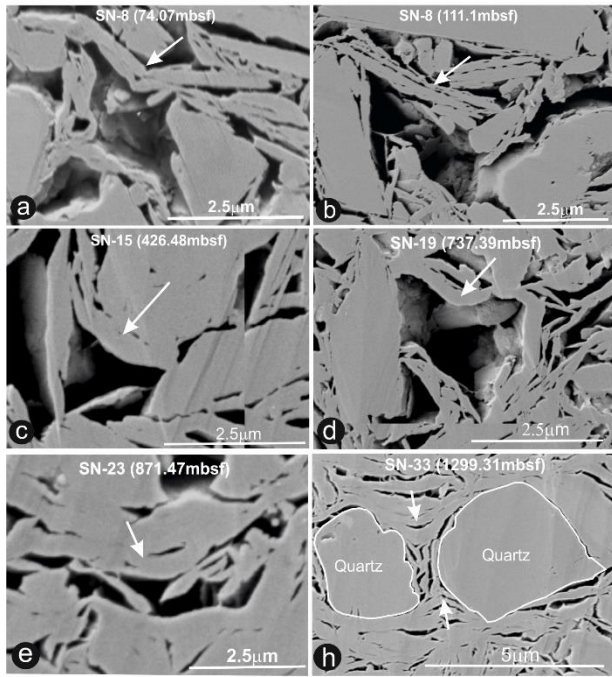
1125

1126 **Fig.12:** (a) Clay content vs difference between MAD and BIB-SEM porosity. **Green, orange and blue colored**
 1127 **symbols represent the samples from Unit-I, II and III respectively.** (b) Multivariate regression analysis using three
 1128 parameters: BIB-SEM porosity, clay content, and MAD porosity (33 samples).

1129

1130

1131



1132

1133 **Fig.13:** a-f: examples of bent clay particles on top of silt-adjacent larger pores; sample ID and depth labelled on
 1134 photos. (g) Micromechanical model for collapse of large silt-adjacent pores.

1135

1136

1137

1138

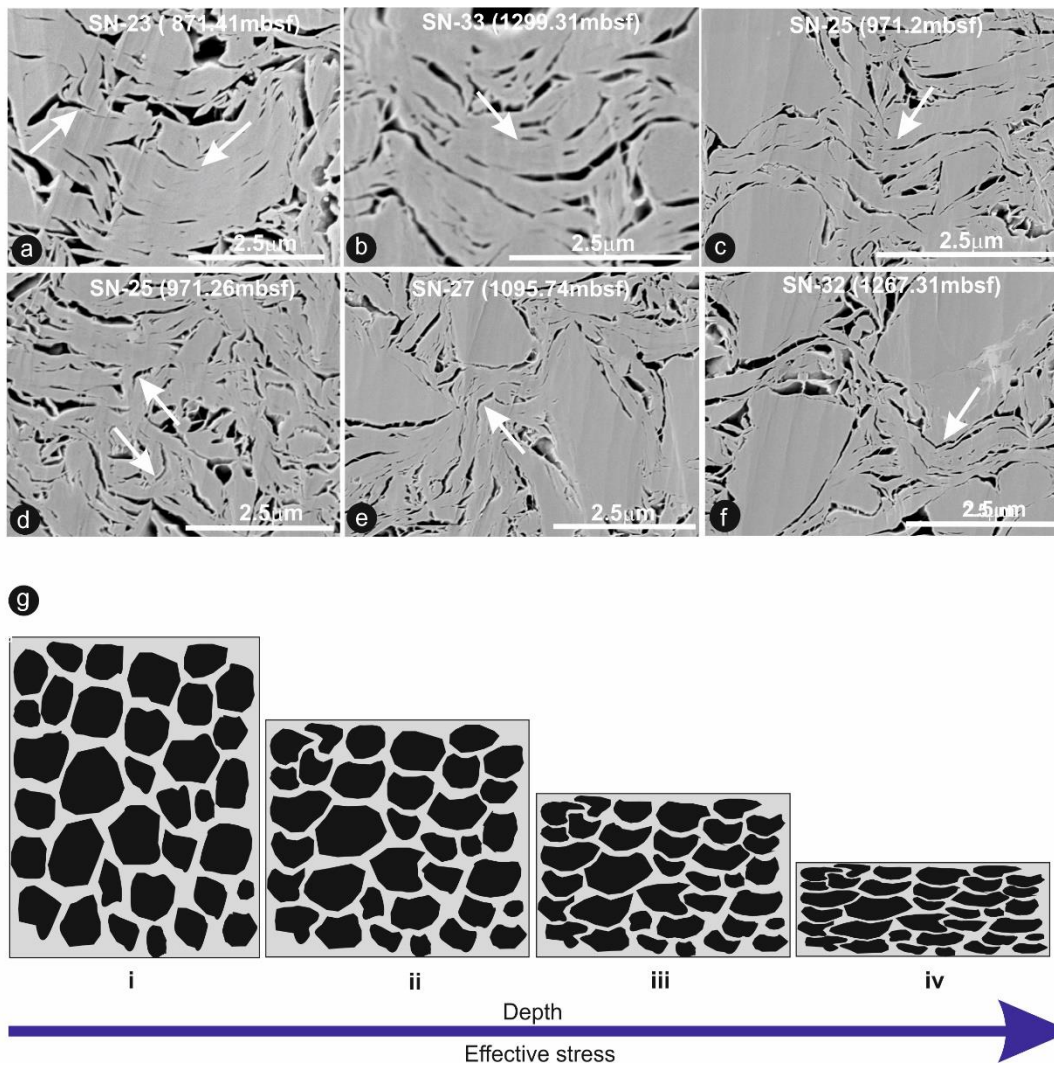
1139

1140

1141

1142

1143



1144

1145 **Fig.14:** a-f: examples of clay aggregate bending (white arrows). (g) Conceptual diagram tracing porosity reduction
 1146 and increase in preferred alignment of the long axes of pores by bending of clay perpendicular to applied vertical
 1147 stress.

1148

1149

1150

1151

1152

1153

1154

Table 1: Core description, bulk mineralogy (McNeill et al., 2017b) and clay composition (Rosenberger et al., 2020) of the analysed samples. Bulk measurements were done shipboard on Expedition 362 (McNeil et al., 2017a; Underwood, 2020). Additional clay mineralogical analysis was done on the <2µm particle fraction onshore using a different instrument and methodology (Rosenberger et al., 2020). Here, Plag= Plagioclase feldspar, Smec= Smectite*, Chl= Chlorite, Kaol= kaolinite, Calc= Calcite.

	Sample no	Site	Hole	Core	Type	Sec	Depth	Unit	Bulk mineralogical comp (XRD)				Clay mineralogical comp (XRD)			
									Total clay	Quartz	Plag.	Calc.	Smec*	Illite	Chl+Kaol	Quartz
First set of sample (Analysed at Aachen university)	SN-1	U1480	E	1	H	1	1.24	I	68	12	9	11	25	58	68	12
	SN-2	U1480	E	1	H	4	5.10	I	67	12	9	12	24	60	67	12
	SN-3	U1480	E	2	H	1	9.18	I	71	15	12	2	38	49	71	15
	SN-4	U1480	E	2	H	2	10.69	I	66	15	10	9	36	59	66	15
	SN-5	U1480	E	3	H	6	26.05	I	62	19	11	8	40	43	62	19
	SN-6	U1480	E	4	H	1	28.00	IIA	63	21	13	3	14	62	63	21
	SN-7	U1480	E	9	H	2	63.24	IIA	64	20	13	3	11	67	64	20
	SN-8	U1480	E	10	H	2	74.07	IIA	65	20	12	3	21	58	65	20
	SN-9	U1480	E	11	H	5	87.98	IIA	60	21	17	2	6	74	60	21
	SN-10	U1480	F	2	H	1	98.25	IIA	63	19	16	2	7	77	63	19
	SN-11	U1480	F	3	H	3	111.10	IIA	67	17	14	2	6	76	67	17
	SN-12	U1480	F	15	F	2	176.50	IIA	62	22	14	2	13	69	62	22
	SN-13	U1480	F	26	F	1	226.70	IIA	70	17	11	2	22	58	70	17
	SN-14	U1480	F	53	X	2	369.19	IIB	68	18	12	2	21	53	68	18
	SN-15	U1480	F	59	X	1	426.68	IIB	68	18	11	3	9	69	68	18
	SN-16	U1480	F	67	X	CC	505.32	IIB	70	17	11	1	30	49	70	17
	SN-17	U1480	F	76	X	1	592.42	IIB	61	24	12	3	22	56	61	24
	SN-18	U1480	F	80	X	CC	630.55	IIB	68	15	14	2	19	59	68	15
	SN-19	U1480	F	91	X	1	737.39	IIB	67	19	12	1	36	46	67	19
	SN-20	U1480	F	92	X	1	751.16	IIB	67	19	12	2	36	46	67	19
	SN-21	U1480	G	4	R	2	776.17	IIB	70	18	12	0	40	39	70	18
	SN-22	U1480	G	7	R	CC	802.55	IIC	62	23	14	2	23	54	62	23
	SN-23	U1480	G	14	R	2	871.87	IIC	66	21	12	2	28	50	66	21
	SN-24	U1480	G	20	R	1	929.81	IIC	67	19	11	3	21	57	67	19
	SN-25	U1480	G	24	R	3	971.26	IIC	66	19	13	1	41	40	66	19
	SN-26	U1480	G	30	R	2	1027.91	IIC	65	22	13	0	21	51	65	22
	SN-27	U1480	G	37	R	2	1095.74	IIC	68	19	12	1	30	51	68	19
	SN-28	U1480	G	41	R	1	1119.70	IIC	69	16	12	3	19	57	69	16
	SN-29	U1480	G	45	R	1	1172.88	IIC	63	21	11	5	22	54	63	21
	SN-30	U1480	G	46	R	3	1184.39	IIC	65	17	12	6	18	57	65	17
	SN-31	U1480	G	51	R	CC	1233.15	IIC	61	23	12	4	17	59	61	23
	SN-32	U1480	G	55	R	6	1267.14	IIIA	68	19	12	1	64	25	68	19
	SN-33	U1480	G	59	R	1	1299.31	IIIA	72	15	12	0	54	36	72	15
Second set of sample (Analysed at BEG)	SN-34	U1480	H	2	H	2	6.25	IB	71	18	11	0	25	54	19	2
	SN-35	U1480	E	1	H	6	7.21	IB	70	12	10	8	24	55	19	2
	SN-36	U1480	H	3	H	1	14.28	IB	62	21	14	3	5	70	9	15
	SN-37	U1480	E	4	H	1	28.12	IIA	63	21	13	2	14	62	11	14
	SN-38	U1480	E	7	H	1	50.82	IIA	61	22	14	3	11	67	15	7
	SN-39	U1480	H	10	H	2	83.02	IIA	59	21	15	4	6	74	10	10
	SN-40	U1480	H	16	H	1	117.13	IIA	62	20	16	2	12	73	11	5
	SN-41	U1480	E	12	H	2	92.82	IIA	59	23	16	2	6	72	9	13
	SN-42	U1480	F	16	F	3	182.62	IIA	64	21	13	2	14	63	16	7
	SN-43	U1480	F	37	X	2	285.51	IIA	66	20	12	2	15	62	19	4
	SN-44	U1480	F	55	X	5	394.01	IIB	58	28	13	0	40	38	13	9
	SN-45	U1480	F	65	X	CC	486.72	IIB	59	26	14	1	30	49	14	7
	SN-46	U1480	F	79	X	1	621.2	IIB	66	19	13	2	19	59	19	4
	SN-47	U1480	F	91	X	1	737.47	IIB	67	19	12	1	36	46	14	4
	SN-48	U1480	G	11	R	1	841.56	IIC	63	22	13	2	26	51	19	4
	SN-49	U1480	G	23	R	1	959.15	IIC	58	26	14	2	33	46	18	3
	SN-50	U1480	G	30	R	1	1026.34	IIC	68	18	12	2	21	51	24	3
	SN-51	U1480	G	42	R	3	1145.91	IIC	60	22	12	5	14	61	18	7
	SN-52	U1480	G	54	R	2	1251.5	IIIA	63	22	13	1	16	53	16	16
	SN-53	U1481	A	23	R	5	1358.9	IIC	68	17	11	3	18	58	20	4
	SN-54	U1481	A	32	R	1	1432.5	IIIA	65	23	11	1	32	46	17	5
	SN-55	U1481	A	38	R	3	1493.3	IIIA	60	26	13	1	20	42	14	24

*Smectite includes all mixed-layer I/S; expandability of mixed-layer I/S determined separately (Rosenberger et al., 2020).